



RESEARCH ARTICLE

10.1029/2024JD043133

Simulation of Tilted Rooftop Photovoltaic Panels at City Scale: Novel Measurements, Model Development, and Application in WRF

Key Points:

- A detailed year-long measurement campaign captures surface-atmosphere exchange for a rooftop array of tilted photovoltaic (PV) panels
- We extend and evaluate a rooftop PV energy balance model, UCRC-Solar, and couple it to the multilayer urban canopy scheme BEP-BEM
- Weather Research and Forecasting simulations over Toronto show more notable daytime warming and less nighttime cooling from tilted than flat rooftop PV panels

Supporting Information:

Supporting Information may be found in the online version of this article.

Correspondence to:

H. Yin and E. S. Krayenhoff,
hyin09@uoguelph.ca;
skrayenh@uoguelph.ca

Citation:

Yin, H., Krayenhoff, E. S., Voogt, J., Heusinger, J., & Aliabadi, A. A. (2025). Simulation of tilted rooftop photovoltaic panels at city scale: Novel measurements, model development and application in WRF. *Journal of Geophysical Research: Atmospheres*, 130, e2024JD043133. <https://doi.org/10.1029/2024JD043133>

Received 9 DEC 2024
Accepted 28 APR 2025

Author Contributions:

Conceptualization: Hang Yin, E. Scott Krayenhoff
Formal analysis: Hang Yin
Funding acquisition: E. Scott Krayenhoff, James Voogt, Amir A. Aliabadi
Investigation: Hang Yin, James Voogt
Methodology: Hang Yin, E. Scott Krayenhoff, James Voogt, Jannik Heusinger
Resources: E. Scott Krayenhoff, James Voogt
Software: Hang Yin, Jannik Heusinger

© 2025 The Author(s).
This is an open access article under the terms of the [Creative Commons Attribution-NonCommercial License](#), which permits use, distribution and reproduction in any medium, provided the original work is properly cited and is not used for commercial purposes.

Hang Yin¹ , E. Scott Krayenhoff¹ , James Voogt² , Jannik Heusinger³ , and Amir A. Aliabadi⁴

¹School of Environmental Sciences, University of Guelph, Guelph, ON, Canada, ²Department of Geography and Environment, University of Western Ontario, London, ON, Canada, ³Institute of Geoecology, Technische Universität Braunschweig, Braunschweig, Germany, ⁴School of Engineering, University of Guelph, Guelph, ON, Canada

Abstract Rooftop photovoltaic (PV) panels alter the urban energy balance and affect local climate. However, the use of simplified PV models and models lacking thorough evaluation against observational data has resulted in conflicting conclusions related to their local climate impacts. Here, we further develop a rooftop PV energy balance model, UCRC-Solar, and couple it to the multilayer urban canopy scheme BEP-BEM in the Weather Research and Forecasting (WRF) model. Model extensions include updated radiative and convective energy exchanges between both sides of the PV module and the atmosphere/roof surface. We conduct a year-long measurement campaign in London, Canada, to provide a comprehensive meteorological and energy balance data set for an array of tilted PV panels on a flat roof. The upgraded UCRC-Solar is evaluated extensively against this newly collected PV module surface temperature and electricity production data, both offline and online. Coupled mesoscale WRF simulations for Toronto, Ontario, showcase the impacts on urban climate from different configurations of rooftop PV models. UCRC-Solar with tilted panels shows the most notable daytime warming ($\sim 1.0^{\circ}\text{C}$) and the least nighttime cooling ($\sim 0.4^{\circ}\text{C}$) of the near-surface air temperature, followed by UCRC-Solar with flat panels, and finally, the existing WRF PV model, which yields more cooling. Unlike previous work at this scale, our approach includes all relevant physical processes and rigorous model evaluation for extended periods across different locations. Furthermore, the updated UCRC-Solar in WRF permits panels with any tilt, which has not previously been available at this scale.

Plain Language Summary City-wide deployment of rooftop photovoltaic (PV) panels has been proposed as an effective mitigation strategy for urban heating since PV panels can shade the underlying surface and generate electricity. However, the effects of PV panels on near-surface air temperature are less conclusive. This study presents an upgraded physics-based rooftop PV numerical model UCRC-Solar and its implementation in the Weather Research and Forecasting (WRF), a widely used numerical weather prediction model. The updated UCRC-Solar is capable of capturing diurnal and seasonal features of PV module surface temperature and electricity power production, both of which are collected from a full-year rooftop campaign at the University of Western Ontario, London, Canada. Moreover, WRF experiments with different PV configurations on flat roofs are explored in Toronto, Ontario. Results suggest that previous WRF experiments with flat PV panels may underestimate the daytime warming penalty and overestimate the nighttime cooling benefit, especially in the summer season. The revised modeling framework enables better quantification of the trade-off between priorities, including heat mitigation, and reduction of building energy consumption and associated greenhouse gas emissions.

1. Introduction

According to Statistics Canada (2024), more than 80% of the population of Canada is concentrated in urban areas, and globally more than half of the population resides in cities (United Nations, 2018). Global climate change and local urban development are projected to result in more frequent, prolonged, and severe heatwaves (Nazarian et al., 2022). As a result, the energy demand for space cooling in buildings is only expected to grow. These trends contribute to a positive feedback loop because electricity production still partially relies upon traditional fossil fuels. In Canada, it is estimated that buildings account for 30–40% of total energy consumption (EC) and 13% of direct greenhouse gas (GHG) emissions (Environment and Climate Change Canada, 2022). Therefore, transitioning to a renewable energy system is crucial to achieving the Government of Canada's net-zero GHG

Supervision: E. Scott Krayenhoff, Amir A. Aliabadi
Validation: Hang Yin
Visualization: Hang Yin
Writing – original draft: Hang Yin
Writing – review & editing: Hang Yin, E. Scott Krayenhoff, James Voogt, Jannik Heusinger, Amir A. Aliabadi

emissions goal by 2050. The adoption of city-wide rooftop photovoltaic panels (RPVP) has been suggested as a favorable option to reduce net building energy use and GHG emissions, especially in temperate climate regions like Canada. However, the climate impacts of PV systems at local to city scales still require further investigation.

Most contemporary commercial PV modules are characterized by crystalline silicon solar cells (Fraunhofer ISE, 2020). Traditional monofacial solar cells collect solar energy solely from the front surface of the module. Bifacial cells, which can harness solar radiation from both sides, have also gained popularity. Commercially available PV modules typically have a low surface albedo (~0.1) and a rated electrical efficiency of ~20% (Silva et al., 2010). Therefore, most of the incident solar radiation is converted to thermal gain. Since PVPs have low thermal mass, they tend to heat up and cool down more rapidly than the surrounding surfaces while shedding the thermal energy to ambient air through convection (Broadbent et al., 2019). Such mechanisms cause the PV surface temperature to rise considerably above ambient air during the day while also staying cooler than the air during the night due to the high sky view factor. In urban environments, PV modules are usually arranged in rows of flat or fix-tilted arrays on rooftops. To minimize the module efficiency loss from overheating, PVPs are often mounted with a certain air gap between the surface beneath for elevated convective heat transfer from the rear side. In addition to the extra (two-sided) surface area that exchanges heat with the atmosphere, photovoltaic systems modify the overall roof energy balance due to their different material properties, partial shading of the roof, impacts on the effective roughness of the roof, and electrical energy generation from solar radiation. Consequently, PV systems can directly affect ambient air temperature and modulate building EC through radiative exchange processes (Sailor et al., 2021). The extent of these effects also varies based on factors such as the time of the day, local climate, and building construction materials.

Broadbent et al. (2019) measured the impacts of PV systems at a utility-scale PV farm surrounded by open shrubland in southern Arizona for 1 year. They found that on average, daytime maximum 1.5 m air temperature is 1.3 K higher in the PV site than the nearby reference site, whereas no significant effect was observed during nighttime. Some mesoscale modeling studies have adopted the so-called “effective albedo” approach, where the original land surface albedo is replaced by the sum of the PV albedo and electricity generation efficiency (e.g., Ma et al., 2017; Millstein & Menon, 2011). However, the results based on such an approach may require reevaluation as the energy exchange from the rear side of the panel is ignored (Sailor et al., 2021). PV energy balance models with different levels of complexity are also used in urban mesoscale studies for city-scale impacts. Masson et al. (2014) developed a simplified PV energy balance model in the Town Energy Balance scheme where the PV surface temperature is estimated based on a linear relationship between air temperature and available shortwave radiation. They found summer daytime and nighttime near-surface air temperature cooling in Paris possibly due to panel sensible heat release being estimated as a residual from the PV energy balance. Using similar assumptions, Salamanca et al. (2016) investigated the impacts of city-scale adoption of RPVP with the multilayer urban canopy scheme BEP-BEM (Martilli et al., 2002; Salamanca et al., 2010) in the Weather Research and Forecasting (WRF) model. They also found near-surface air temperature and space-cooling energy reduction in Phoenix and Tucson. Recently, Zonato et al. (2021) introduced a full energy balance RPVP model in WRF and suggested that RPVP can increase daytime air temperature in summer and winter, but decrease summer nighttime air temperature. However, all the above modeling studies only considered flat panels parallel to flat roof surfaces and the PV models used often lacked systematic evaluation against observations. Heusinger et al. (2021) adapted a utility-scale PV energy balance model, UCRC-Solar (Heusinger et al., 2020), for urban rooftop applications. The base model has been evaluated against measurements from a utility-scale array in Arizona (Broadbent et al., 2019; Heusinger et al., 2020) and the rooftop model with measurements from an urban rooftop PV array in Braunschweig, Germany (Heusinger et al., 2021) and showed considerable differences between flat and tilted PV systems at the building scale, especially during winter seasons. Regardless, the effects of tilted PV panels at the city scale have not yet been explored.

In this study, we present an upgraded version of the rooftop photovoltaic energy balance model UCRC-Solar, now revised to permit tilted panels. This new version accounts for mutual shading between adjacent PV rows, radiation exchange with improved view factor calculations, and new options for convective heat transfer. A detailed measurement campaign is carried out for a rooftop array of tilted PV panels at the University of Western Ontario (UWO) over a full year to provide new data for model evaluation. The newly evaluated model is subsequently coupled to the multi-layer BEP-BEM scheme in WRF to investigate the adoption of RPVP at the city scale. Mesoscale simulations with UCRC-Solar and WRF-PVP were run to compare the two rooftop PVP schemes on

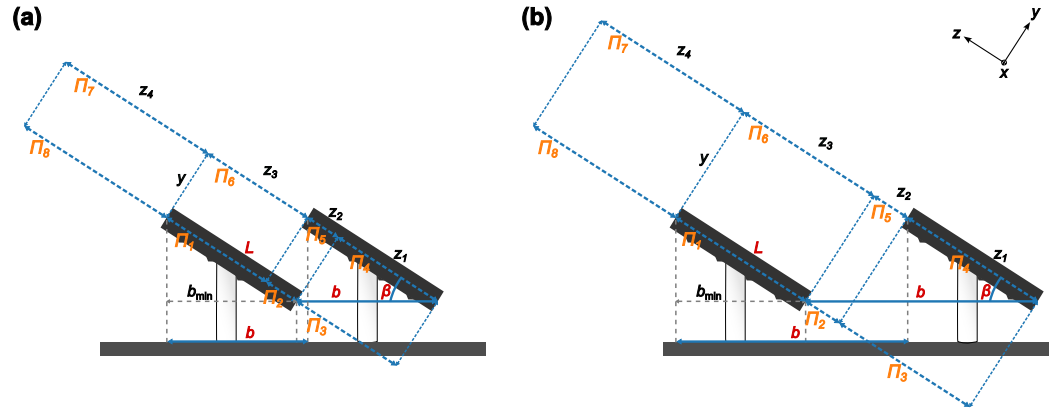


Figure 1. Schematics of tilted PV-roof-sky view factor calculation when the horizontal distance between two adjacent PV rows (b) is (a) $b < \frac{L}{\cos(\beta)}$ or (b) $b \geq \frac{L}{\cos(\beta)}$. L and β are the length and the tilt angle of one PV module, respectively. Π_i represents plane i by z_i and the length of one PV row x (into the page). The distance between two adjacent PV row planes is $y = b \sin(\beta)$ and the minimum row distance is $b_{\min} = L \cos(\beta)$.

the effects of near-surface air temperature and building energy use during a contemporary summer and a winter period in Toronto, Canada.

2. Model Description of UCRC-Solar

The energy balance equation of the PV module is based on Jones and Underwood (2001):

$$C_{\text{module}} \frac{dT_{\text{pv}}}{dt} = SW_{\text{tot}} + LW_{\text{pv}}^* - Q_{H,\text{pv}} - P_{\text{out}}. \quad (1)$$

Here, C_{module} is the heat capacity per unit area of the module ($\text{J K}^{-1} \text{m}^{-2}$), T_{pv} is the module surface temperature (K), SW_{tot} is the total shortwave radiation received by the upper surface of the module (W m^{-2}), LW_{pv}^* and $Q_{H,\text{pv}}$ are the net longwave radiation and sensible heat flux on both sides of the module (W m^{-2}), respectively, P_{out} is the electricity power production (W m^{-2}), and dt is the model time step (s).

The heat capacity of the module is defined as the sum of the heat capacity of each individual layer, usually composed of a glazing, a cell, and a backing layer. The model design is kept as monofacial solar cells to avoid complications in multiple shortwave radiation reflection calculations. Below we introduce the updates in the new model version in detail.

2.1. View Factor Calculation

All radiative emission and reflection is assumed to be isotropic and tracked with view factors. Since PV modules are usually arranged in rows of fixed-length arrays, a new view factor calculation scheme for parallel surfaces is introduced (Hottel & Sarofim, 1967; Sparrow, 2018; Wu, 1995). The planes occupied by the PV surfaces are divided into 8 patches (Π_i). Figure 1 shows the two possible geometric schematics based on the PV row spacing. Consequently, view factor from PV to PV ($\Psi_{\text{pv} \rightarrow \text{pv}}$) is determined analytically by the PV module length (L), length of one PV row (L_{row}), spacing between two adjacent PV rows (b), and the tilt angle of the module (β), analogous to the approach of Krayenhoff and Voogt (2007). PV sky view factors from either side ($\Psi_{\text{pv}\uparrow \rightarrow \text{sky}}$, $\Psi_{\text{pv}\downarrow \rightarrow \text{sky}}$) are found similarly by assigning a very large length to the sky patches Π_7 and Π_8 , that is, $z_4 = 10^9 \text{ m}$. The roof view factor from either side of the PV surface is calculated from the summation rule:

$$\Psi_{\text{pv} \rightarrow \text{rf}} = 1 - \Psi_{\text{pv} \rightarrow \text{pv}} - \Psi_{\text{pv} \rightarrow \text{sky}}. \quad (2)$$

Finally, the PV view factor from the roof is determined from the reciprocity relation:

$$\Psi_{rf \rightarrow pv} = \left(\frac{A_{pv}}{A_{rf}} \right) \Psi_{pv \rightarrow rf}. \quad (3)$$

Here, the surface area fraction of the PV relative to the roof is derived from

$$\frac{A_{pv}}{A_{rf}} = \frac{L}{b}. \quad (4)$$

In the case of flat panels on flat roofs, that is, $\beta = 0^\circ$, view factor calculation is simplified to

$$\begin{aligned} \Psi_{pv \uparrow \rightarrow rf} &= \Psi_{pv \downarrow \rightarrow sky} = \Psi_{rf \rightarrow pv \uparrow} = \Psi_{pv \rightarrow pv} = 0.0, \\ \Psi_{pv \uparrow \rightarrow sky} &= \Psi_{pv \downarrow \rightarrow rf} = 1, \\ \Psi_{rf \rightarrow pv \downarrow} &= \frac{L}{b}, \Psi_{rf \rightarrow sky} = 1 - \frac{L}{b}. \end{aligned} \quad (5)$$

2.2. Shortwave Radiation

In Heusinger et al. (2021), total shortwave radiation received by the upper side of the PV module is defined as follows:

$$SW_{tot} = \left(SW_{dir} \cdot \underbrace{\left(\frac{\cos(\theta_h)}{\cos(\theta_{zh})} \right)}_I + SW_{diff} \cdot \underbrace{\left(\frac{1 + \cos(\beta)}{2} \right)}_{II} + SW_{\downarrow} \cdot \alpha_{rf} \cdot \underbrace{\left(\frac{1 - \cos(\beta)}{2} \right)}_{III} \right) \cdot (1 - \alpha_{pv}), \quad (6)$$

where SW_{dir} and SW_{diff} are the direct and diffuse portions received by a horizontal surface from the total downwelling shortwave radiation (SW_{\downarrow}). α_{rf} is the albedo of the roof surface. θ_h , θ_{zh} , and β are the incidence angle of the direct beam ($^\circ$), zenith angle ($^\circ$), and tilt angle of the module ($^\circ$), respectively. Finally, α_{pv} is the albedo of the upward surface of the module. Term I is the geometric factor that represents the ratio of the direct solar beam on a tilted surface to that on a horizontal surface, whereas terms II and III are the view factors from an unobstructed upper PV surface to the sky and to the roof, respectively. Therefore, Equation 6 is only valid for a single PV row or wide-spaced PV solar farms that lack the need to account for shading loss. In a multi-row PV layout on the building roof, however, shadow effects from adjacent rows and to the underlying roof surface have to be considered due to limited available plan areas. Given that south-facing solar panels with an optimal tilt angle tend to be the most efficient in electrical energy production in the northern hemisphere (e.g., Rowlands et al., 2011), the relative shadow height (h_{shad}) and length (l_{shad}) for such oriented panels are adopted from Appelbaum and Bany (1979):

$$h_{shad} = 1 - \left(\frac{\cos(\theta_{zh})}{\cos(\theta_h)} \right) \left(\frac{b}{L} \right), \quad (7)$$

$$l_{shad} = 1 - \left(\frac{\sin(\theta_{zh}) |\sin(\gamma_{sh})| \sin(\beta)}{\cos(\theta_h)} \right) \left(\frac{b}{L_{row}} \right), \quad (8)$$

to simplify geometric relations. Here, γ_{sh} is the solar azimuth angle ($^\circ$) defined from -90° to 90° . The relative shaded area is $A_{shad} = h_{shad} \cdot l_{shad}$.

In contrast to the ideal case where global shortwave radiation (SW_{\downarrow}) is considered for reflection gain to the panels from the roof, the roof-reflected solar radiation (SW_{ref}) is also modified to include the shading effect of PV panels:

$$SW_{ref} = (SW_{dir} \cdot (1 - R_{shad}) + SW_{diff} \cdot (\Psi_{rf \rightarrow sky})) \cdot \alpha_{rf}, \quad (9)$$

where the shaded roof fraction is adapted from Varga and Mayer (2021):

$$R_{\text{shad}} = \frac{L \cos(\beta) + L \sin(\beta) \cdot (\tan(\theta_{zh}) \cos(\gamma_{sh}))}{b}. \quad (10)$$

With the new view factor calculation scheme, Equation 6 is updated to

$$SW_{\text{tot}} = \left(SW_{\text{dir}} \cdot \left(\frac{\cos(\theta_h)}{\cos(\theta_{zh})} \right) \cdot (1 - A_{\text{shad}}) + SW_{\text{diff}} \cdot (\Psi_{\text{pv}\uparrow \rightarrow \text{sky}}) + SW_{\text{ref}} \cdot (\Psi_{\text{pv}\uparrow \rightarrow \text{rf}}) \right) \cdot (1 - \alpha_{\text{pv}}). \quad (11)$$

The albedo of the upper surface of the panel varies across the day based on Fresnel's law of reflection and the index of refraction of the glazing. More details on the determination of α_{pv} can be found in Chapter 5 of Duffie and Beckman (1980).

2.3. Longwave Radiation

The net longwave radiation on the PV module is re-formulated to include one-time reflection from other surfaces:

$$\begin{aligned} LW_{\text{pv}}^* = & \underbrace{LW_{\downarrow \rightarrow \text{pv}} + LW_{\downarrow \rightarrow \text{rf} \rightarrow \text{pv}} + LW_{\downarrow \rightarrow \text{pv}' \rightarrow \text{pv}}}_{\text{I}} \\ & + \underbrace{LW_{\text{rf} \rightarrow \text{pv}} + LW_{\text{rf} \rightarrow \text{pv}' \rightarrow \text{pv}}}_{\text{II}} \\ & - \underbrace{LW_{\text{pv}} + LW_{\text{pv} \rightarrow \text{pv}' \rightarrow \text{pv}} + LW_{\text{pv} \rightarrow \text{rf} \rightarrow \text{pv}}}_{\text{III}} \\ & + \underbrace{LW_{\text{pv}' \rightarrow \text{pv}}}_{\text{IV}} \end{aligned} \quad (12)$$

Here, LW_{\downarrow} is the downwelling longwave radiation from the sky and $LW_{\text{pv}'}$ represents the longwave emission from adjacent PV modules. Term I represents the absorption of direct incident and roof- or PV-reflected downwelling longwave radiation. Term II is the total contribution of the longwave emission from the roof, whereas term III is that of the PV itself. Term IV is the absorption of adjacent PV longwave emission. Since the front and rear sides of the PV module are involved in the longwave radiation exchange, each term includes contributions from both surfaces. The detailed equation with view factor and surface emissivity is given in Supporting Information S1.

2.4. Sensible Heat Flux

The sensible heat flux is

$$Q_{H,\text{pv}} = (h_c^{\uparrow} + h_c^{\downarrow}) \cdot (T_{\text{pv}} - T_{\text{air}}), \quad (13)$$

where h_c^{\uparrow} and h_c^{\downarrow} are the convective heat transfer coefficients ($\text{W m}^{-2} \text{K}^{-1}$) for the front and rear sides of the module. Similar to the original UCRC-Solar model version, the Thermal Analysis Research Program or TARP scheme (Walton, 1983) is used to calculate the convective heat transfer coefficient, but slight modifications are applied. Here, a forced (h_f) and a natural (h_n) component on both sides of the module are used:

$$h_c = h_f + h_n. \quad (14)$$

The forced convection component is based on Sparrow et al. (1979):

$$h_f = 2.537 W_f R_f \left(\frac{PU}{A} \right)^{\frac{1}{2}}, \quad (15)$$

where the wind direction modifier W_f is set to 1.0. P and A are the perimeter (m) and the surface area (m²) of one PV module. (Tests were also done with the dimension of one row of PV modules, but inferior results were obtained.) U is the horizontal wind speed (m s⁻¹) and a minimum threshold of 0.5 m s⁻¹ is applied for exchange coefficient computations. One of the major differences between flat and tilted rooftop PV systems is the distance between the PV module and the roof and the support structure on the rear side of the module, which could have major impacts on sensible heat release and the value of the surface roughness multiplier, R_f . Flat PV modules tend to be installed closer to the roof than tilted ones. For example, the PV site in Germany consists of parallel arrays to the roof with a ~10 cm distance in between which leads to R_f values of 1.0 (Heusinger et al., 2021). Here, the tilted PV arrays at UWO are raised approximately 2.0 m above the roof surface leading to more efficient convective heat exchange. As a result, the effective roughness multiplier R_f is set to 1.1 (smooth) and 2.0 (rough) for the front and back sides of the tilted panels, and to 1.0 (very smooth) for both sides of the flat panels, to account for the installation structure variability (Walton, 1981).

The natural convective coefficient is taken from Walton (1983). For the front side when $T_{pv} - T_{air} > 0.0$ or the rear side when $T_{pv} - T_{air} < 0.0$, it is formulated as follows:

$$h_n = \frac{9.482|T_{pv} - T_{air}|^{\frac{1}{3}}}{7.282 - |\cos(\beta)|}. \quad (16)$$

For the front side when $T_{pv} - T_{air} < 0.0$ or the rear side when $T_{pv} - T_{air} > 0.0$, the natural convective coefficient is

$$h_n = \frac{1.810|T_{pv} - T_{air}|^{\frac{1}{3}}}{1.382 + |\cos(\beta)|}. \quad (17)$$

2.5. Electrical Power Production

Modeled electricity production is kept as in Heusinger et al. (2020):

$$P_{out} = SW_{cell} \cdot \eta_{pv} \min[1, 1 - \eta_{ref}(T_{pv} - 298.15)], \quad (18)$$

where η_{pv} is the rated efficiency of the PV module calibrated at the reference temperature of 25°C and solar radiation of 1000 W m⁻². The working efficiency is assumed to vary linearly with the module temperature. The temperature coefficient, η_{ref} , is usually between 0.2%°C⁻¹ and 0.5%°C⁻¹ for silicon PV modules (Kaldellis et al., 2014). Similar to SW_{tot} in Equation 11, shortwave radiation transmitted through the glazing layer and absorbed by the cell surface is modified to:

$$\begin{aligned} SW_{cell} = M \cdot & \left(SW_{dir} \cdot \left(\frac{\cos(\theta_h)}{\cos(\theta_{zh})} \right) \cdot (1 - A_{shad}) \cdot (\pi\alpha)_{dir} \right. \\ & + SW_{diff} \cdot (\Psi_{pv\uparrow\rightarrow sky}) \cdot (\pi\alpha)_{diff} \\ & \left. + SW_{ref} \cdot (\Psi_{pv\uparrow\rightarrow rf}) \cdot (\pi\alpha)_{ref} \right). \end{aligned} \quad (19)$$

Here, M is the air mass modifier after King et al. (2004) and $(\pi\alpha)$ is the transmissivity-absorptance product of the glazing for direct, diffuse, and roof-reflected solar radiation (Duffie & Beckman, 1980).

3. Measurement Campaign and Model Evaluation

3.1. Site Description and Instrumentation Setup

To collect meteorological data for a rooftop array of tilted photovoltaic modules, we conducted a detailed measurement campaign from 21 September 2023 to 25 September 2024. The campaign was carried out on the roof of the Amit Chakma Engineering Building (ACEB; 43°00' 14.34" N 81°16' 34.54" W) at the University of Western Ontario (UWO), London, Canada. The ACEB is aligned approximately north-south (356–176°) and has

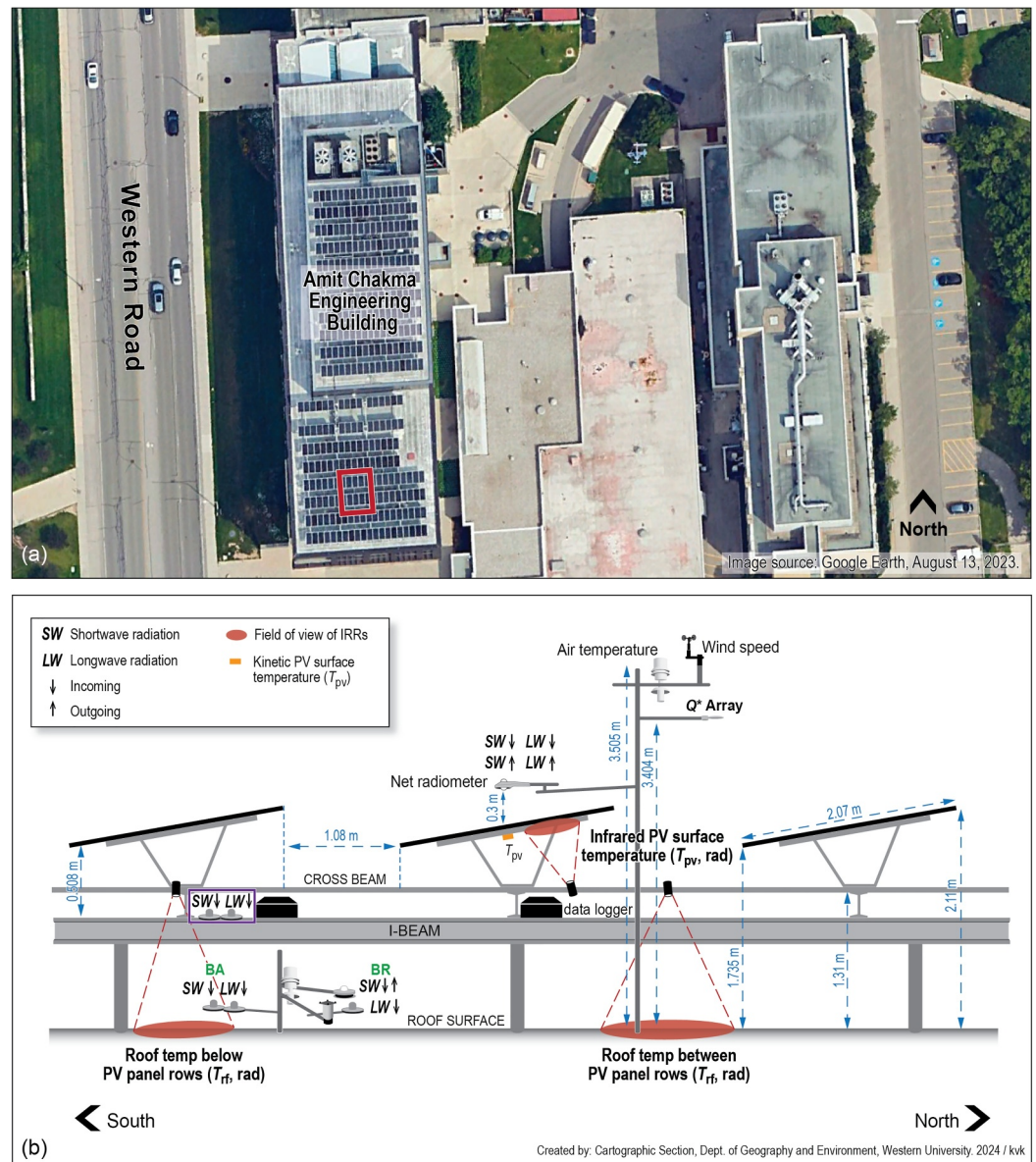


Figure 2. (a) Aerial image of the ACEB (Amit Chakma Engineering Building) on the campus of University of Western Ontario showing the dense PV array mounted on the upper and lower roofs (Imagery from Google Earth (2023)). The red rectangle denotes the area where measurements were made. (b) Cross section of the measurement setup.

a two-level roof, with both roofs covered by dense PV arrays. The array on the lower roof (top of the 4th floor, southernmost part of the roof) consists of 6 rows of PV panels at a fixed angle (14° , south aspect) along with two rows of panels that are mounted in a frame that allows the PV panel angle to be manually set at a select number of angles. The building roof surface is a modified bituminous membrane on a structural steel deck. The surrounding buildings are of equal or lower heights. The PV arrays are composed of 331 LG Electronics LG-385 bifacial solar panels. The panels are grouped into 3 sections serviced by Sungrow and Fronius inverters.

Measurements were made near the middle of the fixed array on the lower portion of the roof (Figure 2a) using two towers, one extending upwards above the array and one located below the PV panels. Measurements of the radiation balance of the PV panel, between row (BR) building roof surface, and below the array (BA) just above the roof surface were made (Figure 2b). Incident short- and longwave radiation was measured directly beneath a PV panel beginning in December 2023 (black box in Figure 2b). Net radiation of the combined PV and building surface was monitored from a tower-mounted sensor. Along with the radiation balance terms, above and below

Table 1
Summary of the Measured Variables in the Campaign

Variable ^a	Unit	Instrument/source	Manufacturer	Model	Uncertainty	Where mounted	Model I/O
– From rooftop setup –							
$SW_{\downarrow}, LW_{\downarrow}$	$W m^{-2}$	4-Component net radiometer	Kipp and Zonen	CNR4	5–20 $\mu V / (W m^{-2})$	Above array	Input
$SW_{\uparrow}, LW_{\uparrow}$							–
$LW_{rf,BA}^{\downarrow}$	$W m^{-2}$	Pyrgeometer	Apogee	SL-510	$\pm 5\%$ (daily total)	Below array	–
$LW_{rf,BR}^{\downarrow}$	$W m^{-2}$	Pyrgeometer	Apogee	SL-510	$\pm 5\%$ (daily total)	Between rows	–
$SW_{rf,BA}^{\downarrow}$	$W m^{-2}$	Thermopile pyranometer	Apogee	SP-510	$\pm 5\%$ (daily total)	Below array	–
$SW_{rf,BR}^{\downarrow}, SW_{rf,BR}^{\uparrow}$	$W m^{-2}$	Thermopile pyranometer	Kipp and Zonen	CMA6	5–20 $\mu V / (W m^{-2})$	Between rows	–
\vec{U}	$m s^{-1}; ^{\circ}$	2D sonic anemometer ^b	RM Young	85,000	$\pm 2\%$ or $\pm 0.1 m s^{-1}$ (speed) $\pm 2^{\circ}$ (direction)	Above array	Input –
		Anemometer ^c	RM Young	Wind Sentry	$\pm 0.5 m s^{-1}$ (speed) $\pm 5^{\circ}$ (direction)		Input –
T_{air}	K	Fine-wire thermistor (aspirated)	Apogee	ST-200	$\pm 0.2^{\circ}C$	Above array	Input
$T_{rf,rad}^{BR}$	K	Infrared radiometer	Apogee	SI-1H1	$\pm 0.2^{\circ}C^f$	Between rows	Input
$T_{rf,rad}^{BA}$	K	Infrared radiometer	Apogee	SI-111	$\pm 0.2^{\circ}C^f$	Below array	Input
T_{pv}	K	Thermocouple	Omega	Type-T	max[$\pm 0.5^{\circ}C, 0.4\%$]	Back of panel	Output
T_{pv}	K	Platinum Resistance PV panel sensor ^d	Campbell Scientific	CS-241	$\pm 0.3–0.4^{\circ}C$	Back of panel	Output
$T_{pv,rad}$	K	Infrared radiometer	Apogee	SI-111	$\pm 0.2^{\circ}C^f$	Below panel	Output
– From other sources –							
Pr	kPa	Nearby weather station	–	–	–	–	Input
P_{out}	kWh ^e	Facilities Management of UWO	–	–	–	–	Output

^aBelow-array air temperature and wind profile were also measured but not used for model evaluation. ^bAdded on 18 June 2024. ^cThe original instrument was a cup and vane but was replaced by just a cup. ^dAdded on 23 May 2024. ^e P_{out} in $W m^{-2}$ is obtained by dividing the data in kWh with surface areas of the PV arrays associated with the inverter. ^fWhen target and detector $\Delta T < 20^{\circ}C$ and $\pm 0.5^{\circ}C$ otherwise.

panel air temperature, wind speed and direction measurements were made as well as the kinetic temperature of the PV panels from a fine wire thermocouple and (later in the project) a back-of-panel platinum resistance thermometer. All variables were recorded every 15 min throughout the campaign, except during equipment malfunction from March 25 to 4 April 2024, and a download error from June 1 to 10, 2024. To track snow presence on the roof, a trail camera was installed on 17 February 2024, although there were some snow events prior to the installation. Hourly local atmospheric pressure (Pr) is obtained from a nearby weather station (WSN; 43°02′00.00″N 81°09′00.00″W, Environment and Climate Change Canada, 2024). A summary of measured variables is listed in Table 1.

3.2. Data Processing

Since the information on the module heat capacity is unavailable, its value is adopted from Jones and Underwood (2001) for the monocrystalline-type cell. Both Euler ($dt = 15 s$) and Newton ($dt = 15 min$) time-stepping schemes were tested. Euler's method solves Equation 1 for module surface temperature prognostically using the heat capacity and needs small time steps (up to 600 s, Table 8 in Heusinger et al. (2020)), whereas Newton's method can adopt a coarser time step ($\sim 30min$) and determines T_{pv} diagnostically assuming negligible heat capacity until temperature differs less than a threshold (0.001 K in our case) between iterations. Given that the model requires direct and diffuse solar radiation as separate inputs, similar to Krayenhoff and Voogt (2007), an hourly diffuse partition model in Chapter 8 of Iqbal (1983) was adopted to determine the diffuse portions (f_{diff}) from measured total downwelling shortwave radiation (SW_{\downarrow}^{obs}). In addition, a clear-sky solar model (Bird & Hulstrom, 1981) was used to calculate the theoretical maximum limit of direct shortwave radiation (SW_{dir}^{max}):

$$\begin{aligned} SW_{\downarrow}^{\text{obs}} &= SW_{\text{dir}}^{\text{obs}} + SW_{\text{diff}}^{\text{obs}}, \\ SW_{\text{dir}}^{\text{obs}} &= \min[(1 - f_{\text{diff}})SW_{\downarrow}^{\text{obs}}, SW_{\text{dir}}^{\text{max}}]. \end{aligned} \quad (20)$$

The calculated albedo of the front surface of the PV module varies between ~ 0.03 (midday) and ~ 0.19 (sunrise/sunset) in February and between ~ 0.03 (midday) and ~ 0.18 (sunrise/sunset) in July in London, Ontario.

To get the true between row or below array roof surface temperature (T_{rf}), the infrared temperature from the sensor ($T_{\text{rf,rad}}$) is corrected from

$$\begin{aligned} \sigma T_{\text{rf,rad}}^4 &= \epsilon_{\text{rf}}\sigma T_{\text{rf}}^4 + (1 - \epsilon_{\text{rf}})\Psi_{\text{sky}}\sigma T_{\text{sky}}^4 + (1 - \epsilon_{\text{rf}})(1 - \Psi_{\text{sky}})\epsilon_{\text{pv}\downarrow}\sigma T_{\text{pv}}^4, \\ T_{\text{rf}} &= \left(\frac{T_{\text{rf,rad}}^4 - (1 - \epsilon_{\text{rf}})\Psi_{\text{sky}}T_{\text{sky}}^4 - (1 - \epsilon_{\text{rf}})(1 - \Psi_{\text{sky}})\epsilon_{\text{pv}\downarrow}T_{\text{pv}}^4}{\epsilon_{\text{rf}}} \right)^{\frac{1}{4}}, \end{aligned} \quad (21)$$

where σ is the Stefan-Boltzmann constant ($\text{W m}^{-2} \text{K}^{-4}$), the sky temperature is acquired from the downwelling longwave radiation, $T_{\text{sky}} = (LW_{\downarrow}/\sigma)^{\frac{1}{4}}$, and the sky view factor (Ψ_{sky}) is obtained from the fisheye images (Figure S1 in Supporting Information S1) with the software RayMan (Matzarakis et al., 2000). It should be noted that the temperatures between rows and below arrays do not directly correspond to sunlit or shaded patterns due to the complex time-varying nature of shade variations, which may lead to some uncertainties in roof surface temperature as an offline model input. The emissivity of the front PV side is measured with a prototype of the emissivity box from Porter and Voogt (2009). Because of the close proximity between kinetic (T_{pv}) and infrared ($T_{\text{pv,rad}}$) temperature of the PV panel, the emissivity of the rear side of the module ($\epsilon_{\text{pv}\downarrow}$) is set to 0.95. Its effect is also ignored in Equation 21 for roof surface temperature correction for simplicity. T_{pv} from the original thermocouple exhibits a minor spike around 17:45 LST, possibly due to its exposure to direct sunlight through the spacing between PV cells. Thus, T_{pv} used for model evaluation is corrected from $T_{\text{pv,rad}}$ before the new platinum resistance PV panel sensor is added on 23 May 2024.

The power output data were provided by the Facilities Management of UWO at 5-min intervals from November to April and at 15-min intervals throughout the rest duration of the measurement campaign. The PV modules have a monofacial efficiency of $\sim 18\%$, whereas additional gain from the rear side at specific tilted angles varies according to solar position. Based on the view factors from the rear side to the sky and to the roof, we estimated that an average of $\sim 10\%$ of bifacial gain is feasible when the PVs are tilted at 14° . Thus, the standard energy conversion efficiency is adjusted to 20% to account for additional rear gain.

The parameters used in the model evaluation run are listed in Table 2. To assess model performance, linear regression between modeled and measured module surface temperature (T_{pv}) and electrical power production (P_{out}) is used to determine systematic model errors; The coefficient of determination (R^2), mean-bias-error (MBE), mean-absolute-error (MAE), and root-mean-square-error (RMSE) were calculated to evaluate goodness-of-fit.

3.3. UCRC-Solar Evaluation

3.3.1. Module Surface Temperature and Power Output

To demonstrate the feasibility of UCRC-Solar under varying solar angles and synoptic weather conditions, we highlight the observed meteorological forcing conditions and model evaluation during a winter month (February) and a summer month (July) in 2024, both featuring mostly clear skies. In February, the observational site records an average air temperature of 0.85°C and a wind speed of 2.06 m s^{-1} . Periodic snowfall events are documented, with the daily minimum air temperature consistently dropping below 0.0°C (Figure A1). During clear-sky days, daily maximum T_{pv} is around 20.0°C and can reach $15.0\text{--}20.0^\circ\text{C}$ warmer than the air; nighttime T_{pv} evolves closely with the ambient air and is often $\sim 3\text{--}4^\circ\text{C}$ cooler. During cloudy conditions, the amplitude of diurnal T_{pv} is much smaller, sometimes staying within $\pm 2^\circ\text{C}$ of the air temperature.

With the PV panels tilted at 14° over flat rooftops, an additional $\sim 30\%$ of direct shortwave radiation gain can be harvested compared to flat panels (Term I in Equation 6, Figure S2a in Supporting Information S1). Figure 3

Table 2
Parameter Setup for UCRC-Solar Evaluation

Parameter	Symbol	Value Unit
– PV and roof properties –		
Module length	L	2.064 m
Module width	W	1.024 m
PV array length	L_{row}	20.48 m
Distance between 2 adjacent PV rows	b	3.083 m
Tilt angle of the module	β	14°
Azimuth angle of the module	γ_h	0°
Upper surface emissivity	$\epsilon_{\text{pv}\uparrow}$	0.90 –
Lower surface emissivity ^a	$\epsilon_{\text{pv}\downarrow}$	0.95 –
Module heat capacity ^a	C_{module}	5,720 J K ⁻¹ m ⁻²
Index of refraction of the glazing layer ^a	n	1.398 –
Solar conversion efficiency at standard test conditions ^a	η_{pv}	20.0%
Solar conversion temperature coefficient	η_{ref}	0.37%
Albedo of the roof surface ^a	α_{rf}	0.2 –
Emissivity of the roof surface ^a	ϵ_{rf}	0.95 –
– Derived view factors –		
From PV to PV	$\Psi_{\text{pv} \rightarrow \text{pv}}$	0.0302 –
From upper side of PV to sky	$\Psi_{\text{pv}\uparrow \rightarrow \text{sky}}$	0.9270 –
From upper side of PV to roof	$\Psi_{\text{pv}\uparrow \rightarrow \text{rf}}$	0.0428 –
From rear side of PV to sky	$\Psi_{\text{pv}\downarrow \rightarrow \text{sky}}$	0.0071 –
From rear side of PV to roof	$\Psi_{\text{pv}\downarrow \rightarrow \text{rf}}$	0.9628 –
From roof to upper side of PV	$\Psi_{\text{rf} \rightarrow \text{pv}\uparrow}$	0.0287 –
From roof to rear side of PV	$\Psi_{\text{rf} \rightarrow \text{pv}\downarrow}$	0.6446 –
From roof to sky	$\Psi_{\text{rf} \rightarrow \text{sky}}$	0.3267 –

^aThe values of these parameters are based on estimation or literature.

shows the observed and modeled PV surface temperature (T_{pv}) and electricity power output (P_{out}) with the Euler time-stepping scheme. UCRC-Solar is able to clearly reproduce the diurnal cycle evolution. The slopes of linear regression of both T_{pv} and P_{out} are close to 1.0, indicating low systematic errors. The values of R^2 , MBE, and RMSE all lie within close range to the previous evaluation results (Heusinger et al., 2020, 2021). The differences between modeled and measured PV surface temperatures are mostly within ± 2 K (gray dashed lines in Figure 3), except during sudden downwelling shortwave radiation fluctuation and heavy snowfall conditions.

Under cloudy conditions, shortwave radiation may be subject to rapid change due to fast-moving clouds, whereas PVP exhibits a lagged thermal response (Jones & Underwood, 2001). Given the daytime energy balance of the tilted PV module is largely driven by the total solar radiation and by its partitioning between direct and diffuse components (Figure S3 in Supporting Information S1), high levels of model sensitivity on T_{pv} are expected when the forcing data are at 15-min interval, as observed during February 12–14 (Figures A1 and 3). These model errors could be attenuated when finer temporal resolution of forcing data are available or when coupled to an atmospheric model.

Starting early on February 17th, a fast-moving snowstorm was reported in London. The continuous snowfall gradually covered the top surface of the PV modules, thereby blocking the absorption and transmission of shortwave radiation to the PV cell. As a result, there was considerable overestimation of both T_{pv} and P_{out} (orange dots in Figure 3). The observed PV surface temperature remained approximately 0.0°C until midday, whereas the

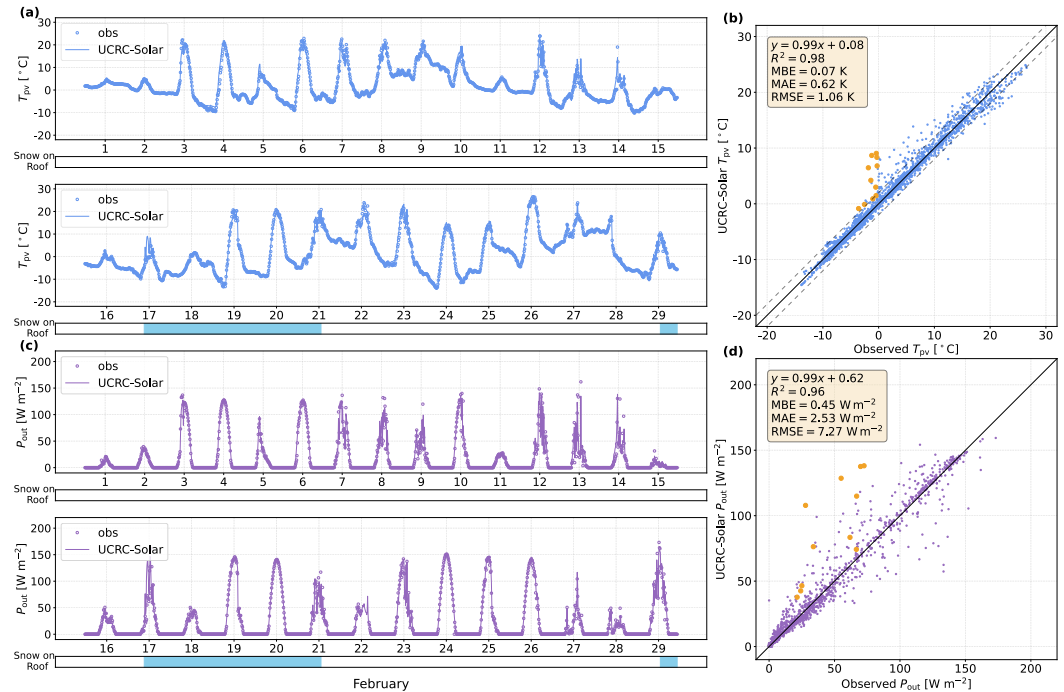


Figure 3. Time series of observed (dots) and modeled (lines) (a) surface temperature (T_{pv}) and (c) electrical power output (P_{out}) of the PV module in February 2024; scatter plot of observed and modeled (b) T_{pv} and (d) P_{out} at 15-min interval for February 2024. Gray dashed lines in (b) indicate observed $T_{pv} \pm 2^\circ\text{C}$. Orange dots in panels (b, d) are during 10:00–12:30 LST on the 17th when the top surface of the PV module is covered by snow.

simulated T_{pv} was substantially higher from presumed solar radiation interactions (Figure 3b). Similarly, UCRC-Solar's prediction on electrical power ($\sim 100 \text{ W m}^{-2}$) was about 2–3 times greater than the observed values ($\sim 50 \text{ W m}^{-2}$) (Figure 3d). Nevertheless, the overestimation quickly diminishes approaching midday when the accumulated snow vacates the panel surface. In the following days, despite the presence of snow on the roof (but not in the model), much higher agreement between observed and simulated values is found. Thus, as long as the snowfall is not heavy and continuous, UCRC-Solar can quickly recover despite its lack of explicit snow treatment. In the rare event of an extended period of snowfall, wherein the upward PV surface may be buried in snow for several days, its temperature can remain well below 0.0°C throughout the daytime with limited electricity production (e.g., January 14–21 in Figure S4 in Supporting Information S1).

July is predominantly characterized by clear-sky conditions with a mean T_{air} of 22.1°C and U of 1.3 m s^{-1} (Figure A2). The average daily solar radiation is around its annual maximum with daylight duration of approximately 15 hr. The PV module surface temperature reaches its daily maximum ($\sim 50.0^\circ\text{C}$) around noon and can be $20.0\text{--}25.0^\circ\text{C}$ higher than the air, whereas nighttime T_{pv} is $\sim 2\text{--}4^\circ\text{C}$ cooler than the ambient air.

The comparison between observed and modeled T_{pv} and P_{out} for July is shown in Figure 4. In contrast to cooler seasons, additional direct shortwave radiation gain from a tilt angle of 14° diminishes to almost zero ($\sim 5\%$) except during early morning and late afternoon (Figure S2b in Supporting Information S1). The values of MBE and RMSE in July are similar to those in February, although a sudden yet consistent spike for T_{pv} is recorded during midday on July 7. A systematic overestimation of P_{out} is observed in the early morning and late afternoon in both July and February. Such outcomes could result from the lack of explicit treatment of the bifacial characteristic of the PV module. However, since the effects are minimal, we argue this trade-off between computational complexity and time and model accuracy is justified, especially on annual and city-wide scales.

3.3.2. Euler Versus Newton Scheme

Figure 5 shows the comparison between Euler's and Newton's time-stepping schemes in four separate seasons. In the winter (DJF), T_{pv} lies within $-20.0\text{--}25.0^\circ\text{C}$, whereas the range rises to $5.0\text{--}60.0^\circ\text{C}$ in the summer (JJA). In

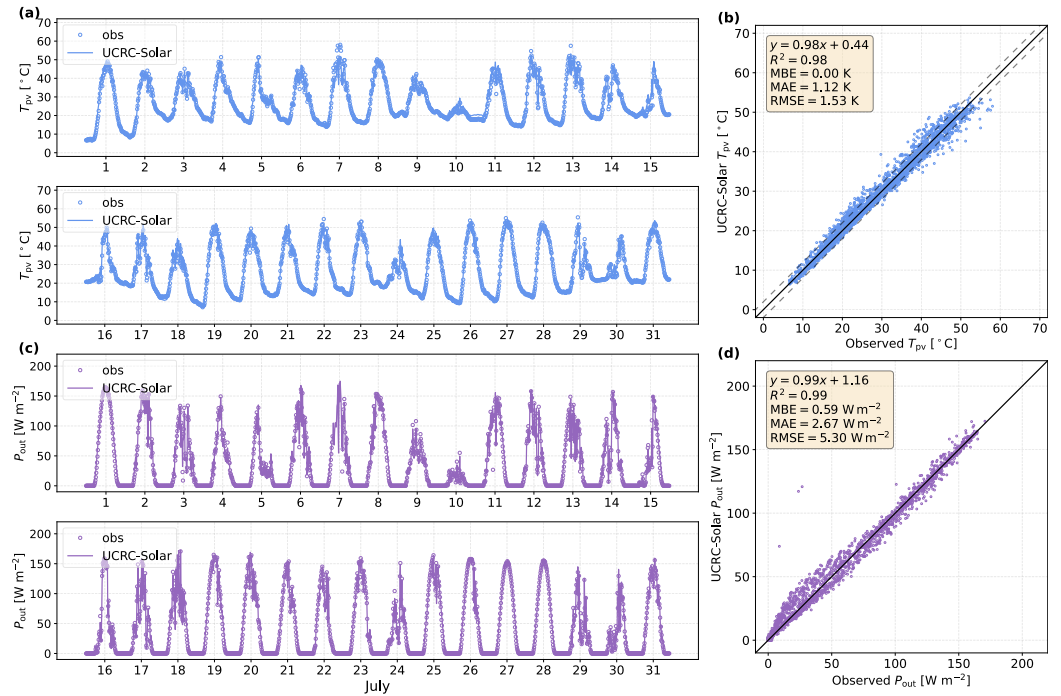


Figure 4. Time series of observed (dots) and modeled (lines) (a) surface temperature (T_{pv}) and (c) electrical power output (P_{out}) of the PV module in July 2024; scatter plot of observed and modeled (b) T_{pv} and (d) P_{out} at 15-min interval for July 2024. Gray dashed lines in panel (b) indicate observed $T_{pv} \pm 2^\circ C$.

shoulder seasons (MAM and SON), T_{pv} falls between -10.0 and $50.0^\circ C$. In general, both methods produce similar metrics, with MBE smaller than $\pm 0.5^\circ C$, MAE smaller than $1.5^\circ C$, and RMSE smaller than $2.0^\circ C$. It is worth noting that Euler's method tends to have smaller MAE and RMSE given its inclusion of the small storage term in energy balance of the PV module. Across four seasons, summer (JJA) exhibits the highest MAE and RMSE values when solar radiation reaches its peak of the year, although the interquartile range normalized RMSE (NRMSE) shows comparable values across all seasons. Such results highlight the importance of solar radiation

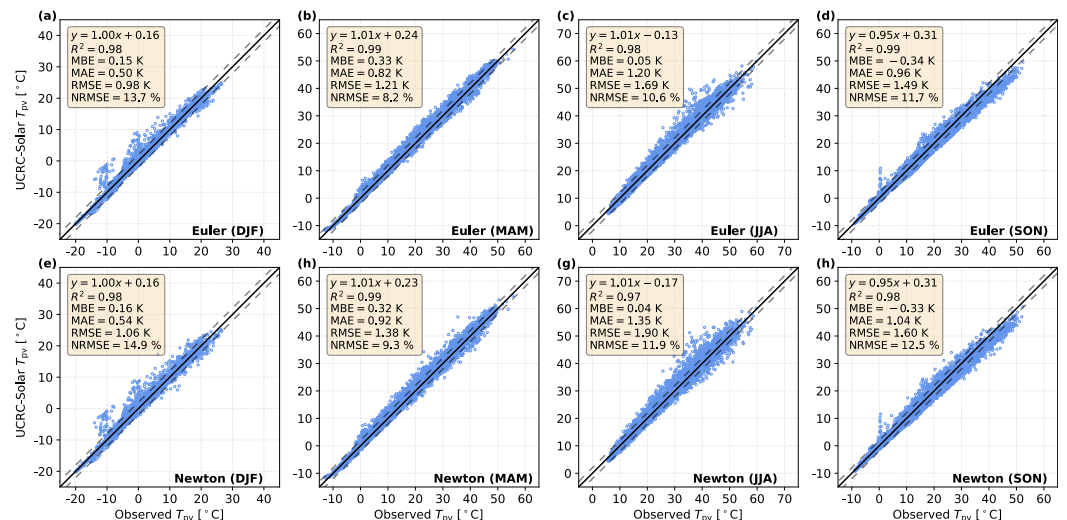


Figure 5. Scatter plots of observed and modeled surface temperature of the PV module (T_{pv}) with (a–d) Euler and (e–h) Newton method for (a, e) December–January–February (DJF), (b, h) March–April–May (MAM), (c, g) June–July–August (JJA), and (d, h) September–October–November (SON).

and is discussed again in Section 4.3.1 for coupled online model evaluation in WRF. In summary, the updated UCRC-Solar is able to effectively capture T_{pv} and its variability across both diurnal and monthly time scales.

In terms of running time, it takes about 1.8 s to run a month of data with the Euler time-stepping scheme at 15-s intervals with Intel i7-8700. With Newton's method, 0.18 s is needed for a full month at a 15-min temporal resolution. Given the fine timestep in WRF ($O \sim 10$ s), we only implemented the Euler method to ensure computational efficiency in the following coupling between UCRC-Solar and BEP-BEM.

4. Model Coupling and Application in WRF

4.1. BEP-BEM-UCRC-Solar Coupling

The newly evaluated model is then coupled to the multi-layer urban scheme BEP-BEM in WRF version 4.3.3 (Skamarock et al., 2019). To enable and run UCRC-Solar, the following input variables for each urban category are needed: plan area density of the PV system on the roof (f_{pv}), length of the PV module (L), tilt angle (β), and the distance between two adjacent PV rows (b). The length of one PV row (L_{row}) is modified from the default 20.0 m to 20.48 m to accommodate the observation site. The coupling procedure between UCRC-Solar and BEP-BEM follows the previous setup by Zonato et al. (2021) with minor modifications of the roof energy balance.

To keep the shortwave treatment of the roof surface consistent between UCRC-Solar and BEP-BEM, total incident solar radiation on the roof follows Equation 9. The direct portion of the incoming longwave radiation to the roof surface is a combination of atmospheric downwelling radiation and downward components emitted by the PV:

$$\begin{aligned} LW_{rf}^{\downarrow} &= LW_{\downarrow \rightarrow rf} + LW_{pv \rightarrow rf}, \\ &= (\Psi_{rf \rightarrow sky})LW_{\downarrow} + (1 - \Psi_{rf \rightarrow sky})\sigma T_{pv}^4. \end{aligned} \quad (22)$$

It should be noted that the shadow patterns and view factors from Equations 9 and 22 are derived with respect to the roof area situated directly beneath or in between the PV rows. In this way, one can neglect the necessity to distinguish the energy balances between sunlit and shaded portions of the roof, thereby keeping an average roof surface temperature. As a result, the relation between b , L , and f_{pv} should strictly follow

$$f_{pv} = \frac{L \cos(\beta)}{b}, \quad (23)$$

to ensure the whole roof is covered by rows of equally spaced solar panels.

Finally, the energy flux to the atmosphere from the RPVP system is the area-weighted sum from both surfaces. For instance, the total sensible heat flux of the system, $Q_{H,tot}$, is computed as

$$\begin{aligned} Q_{H,tot} &= Q_{H,rf} + \left(\frac{A_{pv}}{A_{rf}}\right) \cdot Q_{H,pv}, \\ &= Q_{H,rf} + \left(\frac{f_{pv}}{\cos(\beta)}\right) \cdot Q_{H,pv}. \end{aligned} \quad (24)$$

4.2. Roof Energy Balance Evaluation

To justify the adoption of an averaged roof surface energy balance in WRF-BEP-BEM, we present the comparison between measured and model formulation of incident shortwave (SW_{rf}^{\downarrow}) and longwave (LW_{rf}^{\downarrow}) radiation on the roof surface beneath the PV arrays.

Depending on the solar position, the pyranometers placed below the PV arrays or between the PV rows may be directly illuminated during the day or not. To demonstrate that the solar radiation received by the roof falls within a reasonable range, the diurnally averaged evolution of SW_{rf}^{\downarrow} in March is shown in Figure 6. Over the month, the portions below-array ($SW_{rf,BA}^{\downarrow}$) are often exposed to the direct solar beam while those between-row ($SW_{rf,BR}^{\downarrow}$) always remain in the shade. As a result, modeled SW_{rf}^{\downarrow} based on Equation 9 lies in the middle, effectively

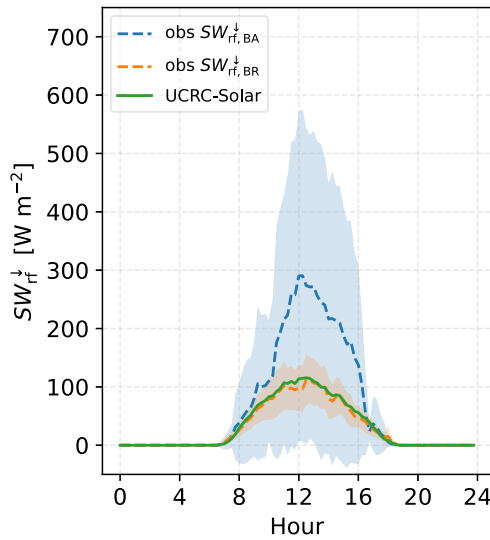


Figure 6. Monthly mean diurnal cycles of the incoming shortwave radiation to the roof in March 2024. The shaded areas represent plus and minus one standard deviation of the mean.

capturing the average condition between sunlit and shaded roof surfaces. During other months, however, both pyranometers may be completely in the shade (e.g., February from Figure S5 in Supporting Information S1), which makes the comparison unfavorable.

The comparison between measured and calculated incident longwave radiation on pyrgeometers placed between-row ($LW_{rf, BR}^{\downarrow}$) or below-array ($LW_{rf, BA}^{\downarrow}$) for March is shown separately in Figure 7. The calculated values are derived using Equation 22, with measured T_{pv} and view factors from Equation 21. Both sets of calculations exhibit a consistent agreement with the observed data. The minor daytime overestimations and nighttime underestimations may result from the misattribution of longwave emissions from ancillary surfaces (e.g., support structure I-beam in Figure 2b) to the PV module. Such surfaces generally have a higher thermal capacity and exhibit a more moderated diurnal temperature fluctuation than the PVP. To verify, thermal images of the RPVP system were taken on 18 June 2024 (Figure S6 in Supporting Information S1). The daytime images suggest that ancillary surfaces could be at 10–15°C cooler than the PV module. Moreover, the absolute discrepancy is relatively minimal ($\sim 15 \text{ W m}^{-2}$), which remains within the operational accuracy of the pyrgeometer (Table 1). The above evaluations of SW_{rf}^{\downarrow} and LW_{rf}^{\downarrow} confirm that the choice of using one energy balance for the roof is reasonable for model coupling in WRF.

4.3. Mesoscale WRF Simulations

4.3.1. WRF-BEP-BEM-UCRC-Solar Model Evaluation

To test and evaluate the coupling procedure and illustrate the impacts of city-wide adoption of different PV implementations, two 10-day simulations with predominately clear-sky conditions, February 3–12, 2024 and July 19–28, 2024, are run for the city of London, Ontario. The initial and boundary conditions are taken from the fifth-generation ECMWF atmospheric reanalysis (ERA5) data at 1-hourly intervals and spatial resolution of 0.25° (Hersbach et al., 2020). Details on the model configuration and land-use data can be found in Jiang et al. (2025). The grid cell at which UWO is located is chosen as the model analysis point.

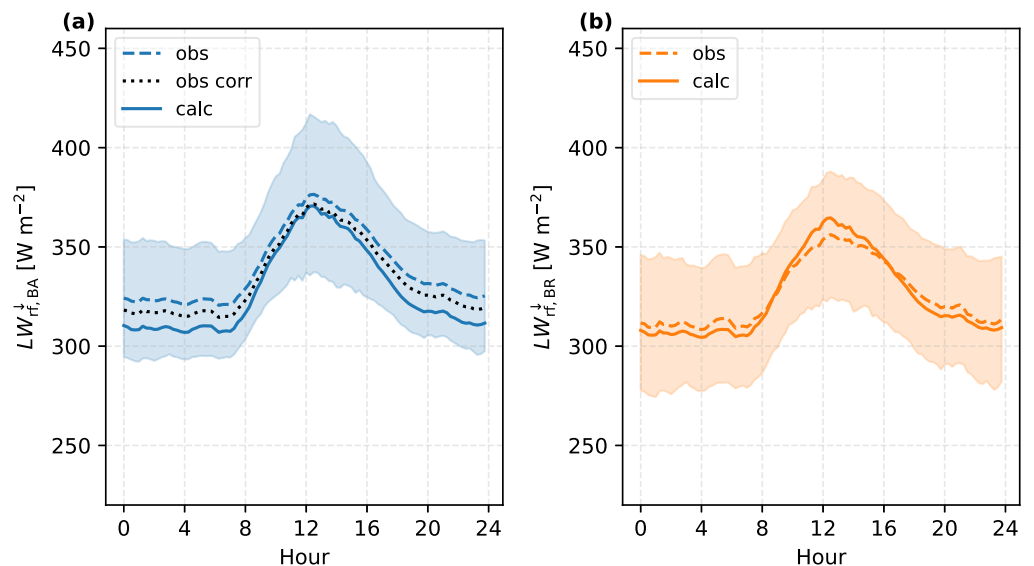


Figure 7. Monthly mean diurnal cycles of the incoming longwave radiation to the (a) below array and (b) between row portion of the roof in March 2024. The shaded areas represent plus and minus one standard deviation of the mean. The black dotted line (obs corr) in panel (a) includes a systemic correction from Stastny et al. (2023) to the original data (obs).

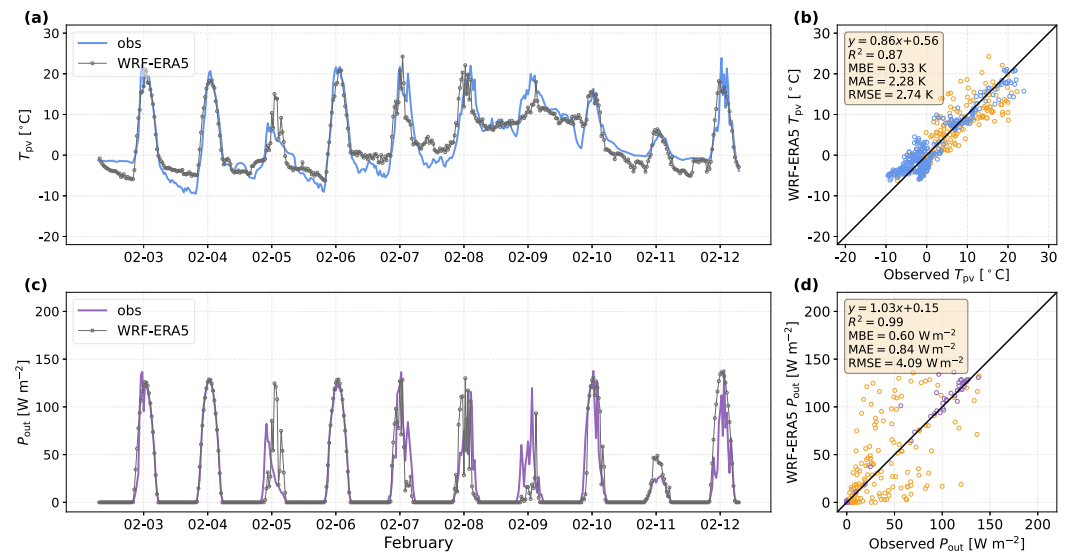


Figure 8. Time series of observed (lines) and Weather Research and Forecasting (WRF) (line with dots) (a) surface temperature (T_{pv}) and (c) power output (P_{out}) of the PV module; scatter plot of observed and WRF (b) T_{pv} and (d) P_{out} at 30-min interval during February 3–12, 2024; orange dots in panels (b, d) indicate conditions when differences between observed and modeled SW_1 are larger than 10.0% (excluded from the statistical metrics calculation).

Figures 8 and 9 show the comparison between the observed and modeled results in the two runs. Given that the energy balance of the PV module is driven by solar radiation during the day, we excluded timestamps when surface solar radiation between observed and model runs are larger than 10% (orange dots in Figures 8 and 9) for statistical metrics calculation. The results show that the coupled model is capable of capturing both diurnal and daily evolution of module surface temperature and electricity production in both seasons reasonably well, provided modeled incoming shortwave radiation is accurate, with a higher sensitivity of P_{out} to local solar conditions. The downgraded statistical metrics compared to the offline evaluations are not issues with the PV model physics or coupling to WRF, rather mainly come from the differences in large-scale ERA5 and point-source meteorological forcing data (e.g., cloud cover), as shown from the comparison of the two in Figures S7 and S8 in

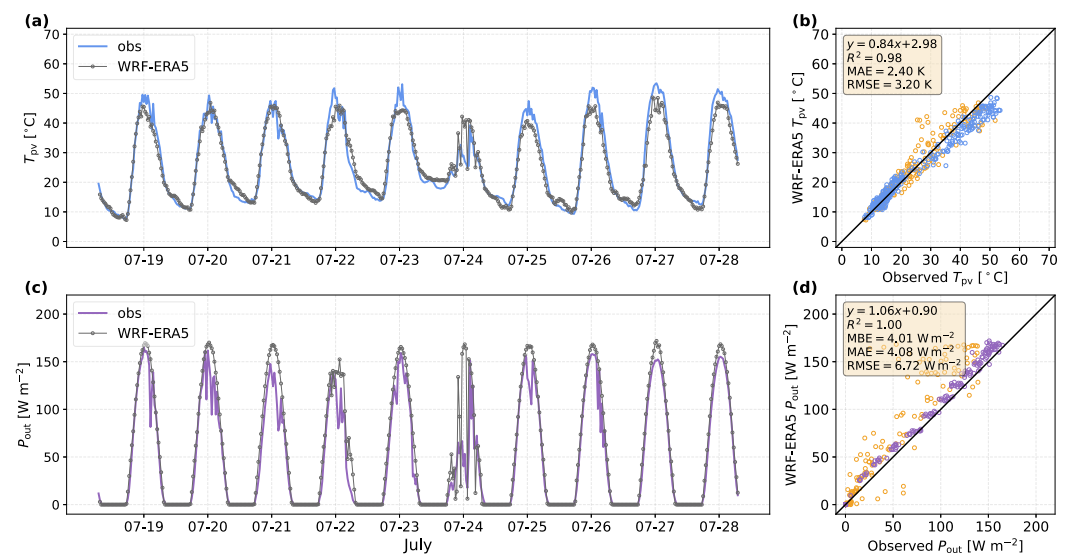


Figure 9. Time series of observed (lines) and Weather Research and Forecasting (WRF) (line with dots) (a) surface temperature (T_{pv}) and (c) power output (P_{out}) of the PV module; scatter plot of observed and WRF (b) T_{pv} and (d) P_{out} at 30-min interval during July 19–28, 2024; orange dots in panels (b, d) indicate conditions when differences between observed and modeled SW_1 are larger than 10.0% (excluded from the statistical metrics calculation).

Table 3
Comparison Between WRF-PVP and UCRC-Solar

Component	Term	WRF-PVP	UCRC-Solar
– PV physics –			
SW_{tot}	α_{pv}	0.11	Varies according to Fresnel's law and index of refraction of the glazing
LW_{pv}^*	$LW_{\text{rf} \rightarrow \text{pv}}$	$h_{\text{rad}} \cdot (T_{\text{rf}}^4 - T_{\text{pv}}^4)^a$	One-time reflection between PV and auxiliary surfaces (Equation 12)
P_{out}	SW_{cell}	SW_{\downarrow}	SW_{\downarrow} transmitted through the glazing and absorbed by the cell surface (Equation 19)
$Q_{H,\text{pv}}$	$h^{\uparrow} + h^{\downarrow}$	DOE-2 model	TARP scheme
– Roof physics –			
R_{rf}	$SW_{\text{rf}}^{\downarrow}$	$(1 - f_{\text{pv}}) SW_{\downarrow}$	Explicit treatment of shading patterns (Equation 9)
	$LW_{\text{rf}}^{\downarrow}$	$(1 - f_{\text{pv}}) LW_{\downarrow} + f_{\text{pv}} \sigma T_{\text{pv}}^4$	With updated view factors from roof to sky and to PV (Equation 22)

$$^a h_{\text{rad}} = \frac{\sigma}{\frac{1 - \epsilon_{\text{pv}}}{\epsilon_{\text{pv}}} + 1 + \frac{1 - \epsilon_{\text{rf}}}{\epsilon_{\text{rf}}}}$$

Supporting Information S1. One can further improve the evaluation metrics by identifying other timestamps with larger differences in ambient air temperature or downwelling longwave radiation. Since our objective is to test UCRC-Solar and its coupling to WRF, rather than whether the whole WRF modeling system accurately captures these observation outputs, we therefore conclude that the coupling is successful and proceed to the final aspect of the model application.

4.3.2. Inter-Model Comparison

To explore the impacts of different rooftop PV models and PV tilt angles on local climate in fully coupled simulations, summer (July 1–18, 2024) and winter (November 27–15 December 2023) cases in contemporary Toronto are simulated with WRF-BEP-BEM with the same model configuration as Jiang et al. (2023). The land-use categories based on local climate zones (LCZs) and urban fractions for the innermost model domain are shown in Figure S9 in Supporting Information S1. ERA5 reanalysis at hourly intervals is taken as the initial and boundary conditions. Model integration starts at 00:00 UTC for 17 days. The last 7 days with predominately clear-sky conditions are chosen as the analysis periods.

A base simulation with no RPVP is conducted as well as three simulations with 100% rooftop PV coverage, each with a different PV model setup: (a) WRF-PVP ($\beta = 0^\circ$, Zonato et al. (2021)), (b) UCRC-Solar flat ($\beta = 0^\circ$), and (c) UCRC-Solar fixed-tilted ($\beta = 14^\circ$). The heat capacity, emissivity, and energy conversion efficiency of the PV modules are set to $5,720 \text{ J K}^{-1} \text{ m}^{-2}$, 0.79 (upward), 0.95 (downward), and 19%, respectively, for all PV simulations, enabling meaningful inter-model comparison. Panel albedo in UCRC-Solar varies based on solar position according to Fresnel's law which differs from the fixed value of 0.11 in WRF-PVP. The differences between each PVP simulation and the base simulation showcase the RPVP effects. A brief summary of the key differences in model physics and parameter inputs is given in Table 3. The two base simulations are evaluated for 2m air temperature in Figures S10 and S11 in Supporting Information S1 with observations from three local weather stations which show comparable results to Jiang et al. (2023).

Figure 10 shows the spatial map of the impacts on near-surface air temperature with different schemes of rooftop solar panels during daytime (a–c) and nighttime (d–f) in July. All experiments indicate moderate differences in temperature change magnitude and spatial extent. According to WRF-PVP, despite a minor warming signal ($\sim 0.4^\circ\text{C}$) near south-west corner of the map, the majority of the urban areas display a clear cooling signal up to $\sim 0.6^\circ\text{C}$ in the daytime. Both UCRC-Solar flat and tilted schemes suggest predominately daytime warming signals, up to $\sim 0.5^\circ\text{C}$ and $\sim 1.0^\circ\text{C}$, respectively. Moreover, the tilted scheme shows greater intensity and geographic spread compared to the flat scheme. During nighttime, all experiments display a cooling signal, up to $\sim 0.8^\circ\text{C}$ in some large low-rise neighborhoods. Nevertheless, the cooling area's spatial extent is diminished in both UCRC-Solar experiments relative to WRF-PVP.

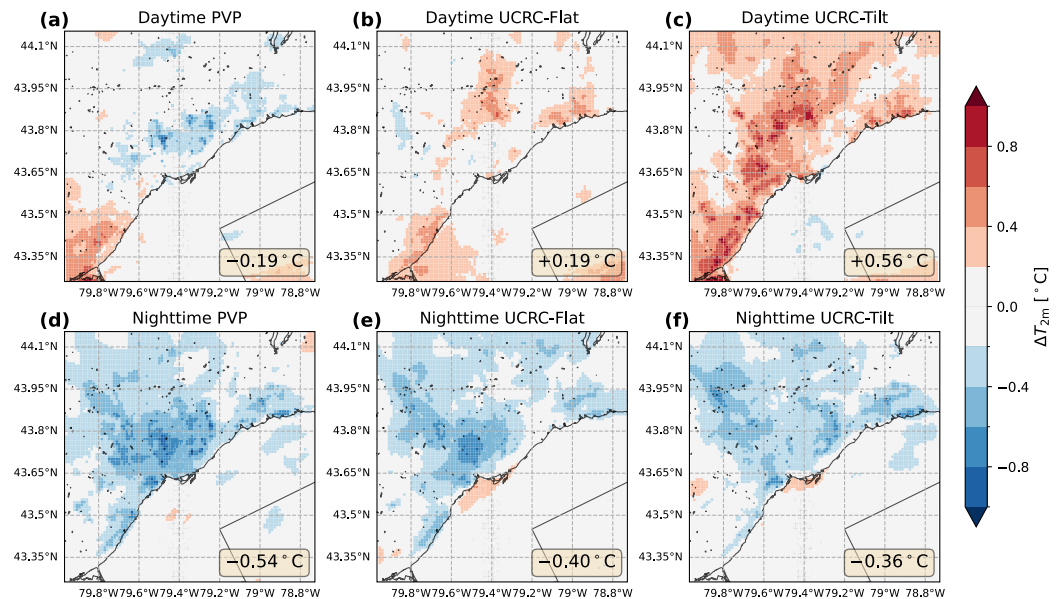


Figure 10. Summertime 7-day averaged 2m air temperature differences (ΔT_{2m}) during daytime (10:00–15:30 LST) between (a) WRF-PVP, (b) UCRC-Solar flat, (c) UCRC-Solar tilt and the reference run in Toronto. Panels (d–f) show the nighttime (22:00–03:30 LST) differences. The numbers denote the average changes for grid cells with urban fraction larger than 0.6.

Across different neighborhoods, Figures 11a–11c show the changes in 2m air temperature in the three dominant urban-type LCZs in Toronto: LCZ1 (compact high-rise), LCZ6 (open low-rise), and LCZ8 (large low-rise). During the daytime, UCRC-Solar tilt shows the largest warming potential over all LCZs, up to $\sim 0.75^\circ\text{C}$ in LCZ1 and LCZ8, followed by $\sim 0.5^\circ\text{C}$ in LCZ6 during 06:00–16:00 LST. UCRC-Solar flat exhibits a more dampened daytime warming extent, especially in LCZ6, whereas WRF-PVP shows almost no change, except a warming spike at 13:00 LST. In contrast to warming, WRF-PVP generally displays a cooling effect, with a peak reduction of $\sim 0.5^\circ\text{C}$ around midnight. The diurnal patterns are less smooth for LCZ1 compared to LCZ6 and LCZ8 possibly due to averaging over a much smaller number of grid cells and the close proximity of LCZ1 neighborhoods to the lake shore in Toronto. These results suggest that current WRF experiments on the adoption of city-wide flat rooftop solar panels may underestimate their daytime warming and overestimate their nighttime cooling potential in the summer, and that tilted panels may further enhance daytime warming and reduce nighttime cooling relative to flat panels. Regarding changes in building energy consumption (EC in Figures 11d–11f), all three PV models show a similar reduction in daytime EC, up to $\sim 0.2 \text{ MW km}^{-2}$ in LCZ6 and $\sim 0.4 \text{ MW km}^{-2}$ in LCZ8 at 16:00 LST. The average daily reduction ranges within 3–19%, in alignment with a previous study in Chicago (Tan et al., 2023). The similar diurnal patterns in EC possibly come from the small variation in roof surface temperature with 100% solar panel coverages and thus the exposure to solar radiation is limited. During the day, electricity generated by the PV panels can sufficiently offset the building energy use in LCZ6 and LCZ8 while it also manages to overcome the peak cooling consumption for LCZ1 (solid lines in Figures 11h and 11i). Caution should be exercised when comparing the absolute power production between the three PV schemes (dashed lines in Figures 11h and 11i) given the simpler treatment of SW_{cell} (equivalent to SW_{\downarrow} , Table 3) in WRF-PVP, although the tilted scheme of UCRC-Solar may potentially outperform WRF-PVP with a more optimal tilt angle.

In terms of changes in grid-averaged surface energy balance terms, the addition of RPVP increases net shortwave radiation (SW^* in Figure 12b) due to the lower panel albedo compared with the underlying roof (0.13 for LCZ1 and LCZ6, 0.18 for LCZ8). Specifically, the lower albedo calculated from UCRC-Solar during the midday (~ 0.03) and the minor additional solar gain from the tilt (5%) lead to higher solar radiation absorption than UCRC-Solar flat and WRF-PVP. Given the low thermal mass and a 19% energy conversion efficiency, surface temperature of the module rises rapidly, exceeding the bare roof in the base simulation, causing an overall decrease in the net longwave radiation (LW^* in Figure 12c). A majority of the thermal gain is then released as sensible heat into the air. Because of the adoption of different forced convection coefficient (h_f) formulations in WRF-PVP (DOE-2 model from Booten et al. (2012)) and UCRC-Solar (TARP scheme), WRF-PVP suggests the least efficient panel sensible heat

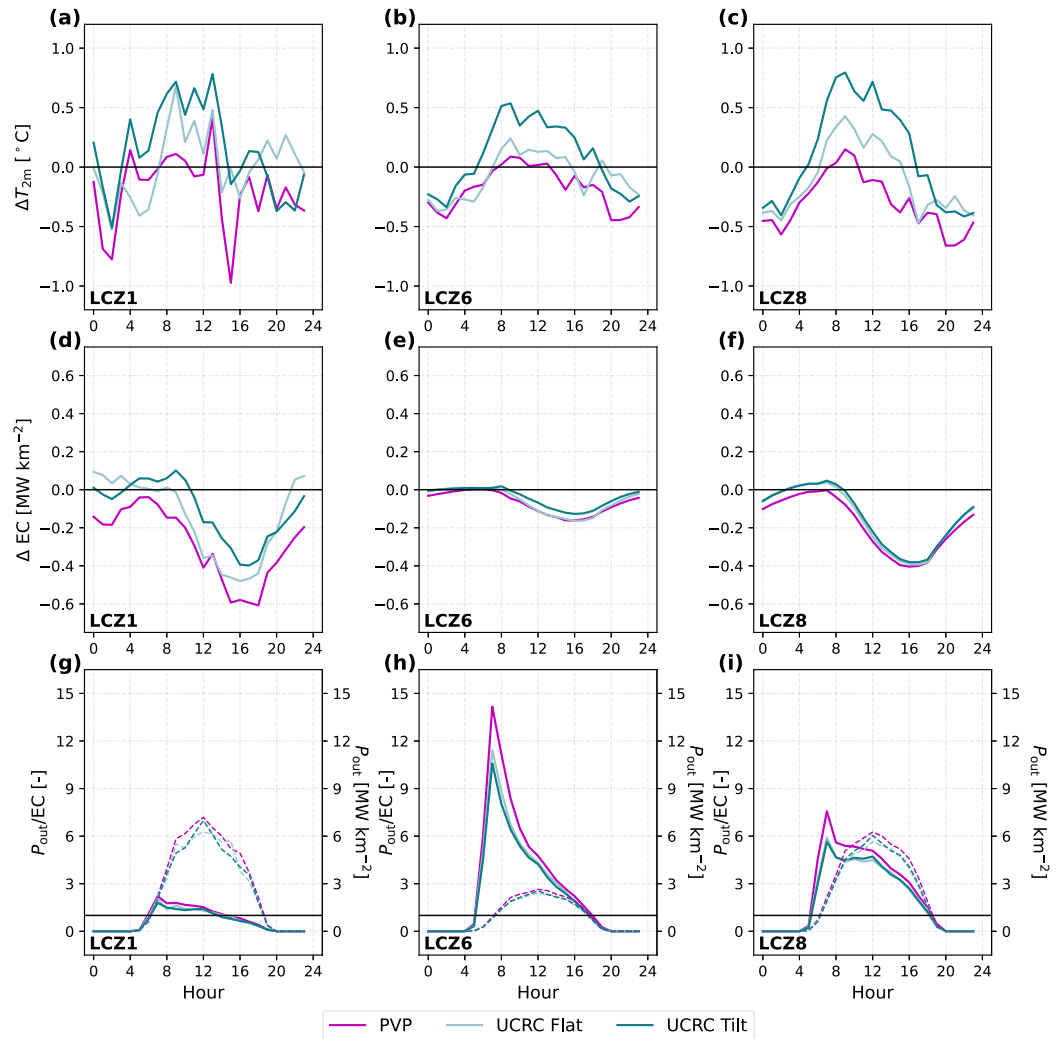


Figure 11. Summertime 7-day averaged differences between rooftop solar panel experiments and the reference run in panels (a–c) 2m air temperature (T_{2m}), (d–f) building energy consumption (EC), and (g–i) PV electricity power production (P_{out} , dashed lines) and the ratio between P_{out} and EC (solid lines) in these experiments in Toronto. Panels (a, d, and g) show the profiles in LCZ1 (compact high-rise), (b, e, and h) in LCZ6 (open low-rise), and (c, f, and i) in LCZ8 (large low-rise).

exchange with ambient air followed by flat and tilted schemes of UCRC-Solar. As a result, a larger diurnal amplitude is observed between the differences of T_{pv} and T_{2m} in WRF-PVP (Figure 12a), which corresponds to peak daytime total Q_H reduction by $\sim 50 \text{ W m}^{-2}$ (Figure 12d). Conversely, both UCRC-Solar flat and tilt increase Q_H by $\sim 70 \text{ W m}^{-2}$ and $\sim 50 \text{ W m}^{-2}$, respectively. It should also be noted that the characteristics of the roof on which PVP is mounted matter; in the case of a cool roof with high albedo, the addition of RPVP can cause an overall increase in both daytime Q_H and EC (Brown et al., 2020). Additionally, variations in latent and ground heat flux (Figures 12e and 12f) are similar among the three, due to limited surface moisture and similar shading patterns on the roof.

In the winter, given a shorter daylight length and the flux density of peak incoming solar radiation is only $\sim 70\%$ of that in the summer, the effects of rooftop PVP on local climates are much smaller (Zonato et al., 2021). All three sets of simulations show almost no change in ambient air temperature ($\pm 0.2^\circ\text{C}$) during both daytime and nighttime over urban areas (Figure S12 in Supporting Information S1). The changes in diurnal cycles of 2m air temperature (Figures S13a–S13c in Supporting Information S1) and energy balance terms (Figure S14 in Supporting Information S1) are around half of those in the summer. It is worth noting that the diurnal cycles of EC are

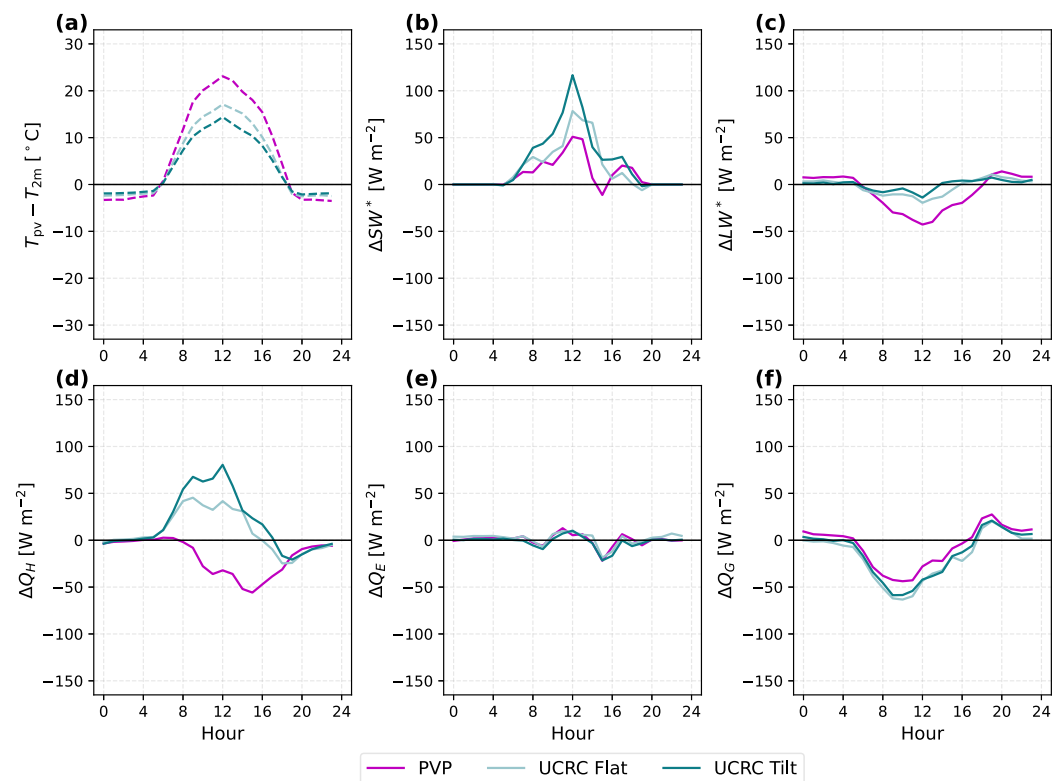


Figure 12. Summertime 7-day averaged (a) differences between module surface temperature and 2m air temperature ($T_{pv} - T_{2m}$) in rooftop solar panel experiments and the differences between these experiments and the reference run in grid-averaged (b) net shortwave radiation (SW^*), (c) net longwave radiation (LW^*), (d) sensible heat flux (Q_H), (e) latent heat flux (Q_E), and (f) ground heat flux (Q_G) for grid cells with urban fraction larger than 0.6 in Toronto.

opposite to those in the summer (Figures S13d–S13f in Supporting Information S1), with a minor daytime increase from shortwave shading and a nighttime decrease from longwave trapping. In addition, electricity production from the PV panels is not able to fully satisfy the heating demand, especially for LCZ1 and LCZ6 (Figures S13g–S13i in Supporting Information S1). Nevertheless, given that the winter season in Toronto is dominated by cloudy conditions, the average effects of RPVP on ambient air and building energy use could be even more attenuated.

5. Discussion

Urban canopy models (UCMs) based on the “urban canyon” concept have been developed and utilized extensively in mesoscale and regional climate models to represent the urban surface and its energy exchange processes with the atmosphere at mesoscale (e.g., Martilli et al., 2002; Masson, 2000). To investigate the impacts of mitigation strategies like rooftop photovoltaic panels, process-based PV models have been developed and coupled to UCMs (Masson et al., 2014; Zonato et al., 2021). Our implementation of UCRC-Solar in BEP-BEM differs from the previous RPVP models at this scale because outputs from UCRC-Solar have been robustly and rigorously evaluated both offline and online for extended periods and for different locations. Furthermore, it offers the option of tilted panels which has not been available in urban environment context.

However, simplification of the urban geometry and morphology has to be made for UCMs to be computationally efficient. For example, all buildings are assumed to have flat roofs in BEP-BEM (Martilli et al., 2002; Salamanca et al., 2010). In real cities, however, most residential neighborhoods have sloped roofs while many light industrial and commercial buildings have more extensive flat roofs. Thus, PV panels parallel to tilted roofs on detached houses are common in contemporary North American cities. Heusinger et al. (2021) demonstrated that such combinations can lead to elevated T_{pv} compared to tilted PV modules over flat, horizontal roof surfaces, due to limited convective heat release from the rear side of the panel. This suggests that the realistic daytime warming

potential with 100% tilted RPVP may not be as large as Figure 10c for Toronto, although this effect could be partially compensated for by higher longwave radiation exchange between the warmer PV surface and the urban atmosphere and nearby urban structures.

We only explored one configuration of 100% rooftop PVP and one tilt angle of 14°, although the fractional variation in RPVP may not exert a linear influence on the local climate due to the complex radiation exchange between the roof and the PV surface. For tilted RPVP, such a high coverage may not be realistic given the direct shading effects from the adjacent PV arrays. However, the optimal layout of the RPVP is beyond the scope of the current study. Furthermore, the solar conversion efficiency of the module is set to 19%, representing the contemporary commercially available PV cells. Nevertheless, recent laboratory research has engineered small-scale PV cells with efficiency as high as 50% (Green et al., 2021). This level of conversion efficiency would limit the PV thermal gain which further changes its modulation of ambient air temperature. In addition, other thermal or radiative properties of the PV module and the underlying roof surface can also modify the energy balance of the combined RPVP system. These aspects introduce uncertainties in quantifying RPVP effects on local cooling or warming potentials and building energy use which calls for a holistic approach to evaluate and prioritize heat mitigation, building EC, and potentially air quality.

6. Conclusion

City-scale deployment of rooftop photovoltaic panels has been proposed as an effective mitigation technology to reduce greenhouse gas emissions, potentially mitigate urban heat, and reduce building energy use by introducing shade on building surfaces. However, application of simplified PV models and models lacking thorough (or any) evaluation against measured data has led to a diversity of conflicting conclusions. Unlike building EC, which is clearly reduced during daytime in summer by rooftop photovoltaic panels according to multiple studies, changes in near-surface air temperature resulting from rooftop PV implementation remain less clear.

To improve the physical representation of rooftop photovoltaic panels (RPVP) and better assess its climate effects at neighborhood and city scales with mesoscale models, we made substantial updates to a rooftop PV model, UCRC-Solar. Significant model extensions including mutual shading from neighboring PV arrays, 3D view factor calculations, detailed longwave radiation exchanges, and updated convective heat transfer coefficients were introduced to account for fixed-tilted solar panels on flat roofs. Due to the lack of high-quality long-term data on RPVP systems, a new measurement campaign was carried out on a rooftop PV installation at the University of Western Ontario in London, Ontario, Canada. The year-long campaign provided a comprehensive data set for the evaluation of a rooftop array of tilted photovoltaic system.

Module surface temperature and electrical power output modeled by the updated UCRC-Solar model performed very well relative to our novel measurements under various climatic conditions. Subsequently, the model was coupled with the multi-layer urban canopy scheme BEP-BEM in WRF and tested again against the same observational data set. Two 10-day, ERA5-driven WRF simulations were run for London, Ontario. Evaluation metrics such as MAE and RMSE for T_{pv} from the WRF runs grew modestly compared to offline results. This is attributed to differences in forcing conditions between local point-sourced observations and the spatially coarser ERA5 reanalysis and subsequent WRF-generated meteorology, particularly the downwelling shortwave radiation and its interaction with clouds, rather than issues with model physics or model coupling.

Finally, WRF simulations were run for Toronto, Ontario with more detailed urban land-use data based on LCZs. In the summer, UCRC-Solar with tilted panels shows the most notable daytime warming ($\sim 1.0^\circ\text{C}$) of the near-surface air temperature among the three experiments, followed by UCRC-Solar with flat panels ($\sim 0.5^\circ\text{C}$), and finally the existing WRF PV model (Zonato et al., 2021). During the nighttime, the opposite trend is found with WRF-PVP exhibiting the most nighttime cooling potentials both in magnitude ($\sim 0.8^\circ\text{C}$) and spatial extent, followed by flat and tilted schemes with UCRC-Solar. Across different urban neighborhoods, compact high-rise (LCZ1) exhibits the largest change in both ambient air temperature and building energy use as a result of rooftop PV implementation, followed by large low-rise (LCZ8), and finally open low-rise (LCZ6). The effects of RPVP on local air temperature in the winter are negligible due to limited solar radiation. We conclude that previous studies may have underestimated daytime warming potential while overestimated nighttime cooling potential

from RPVP during summer. Such results are highly sensitive to the convective heat transfer formulation in the PV model and more sensitivity experiments are needed to better quantify the impacts of the variety of RPVP systems on local urban climate.

Appendix A: Meteorological Conditions

Figures A1–A2 show observed meteorological conditions at 15-min intervals during February 2024 and July 2024, respectively.

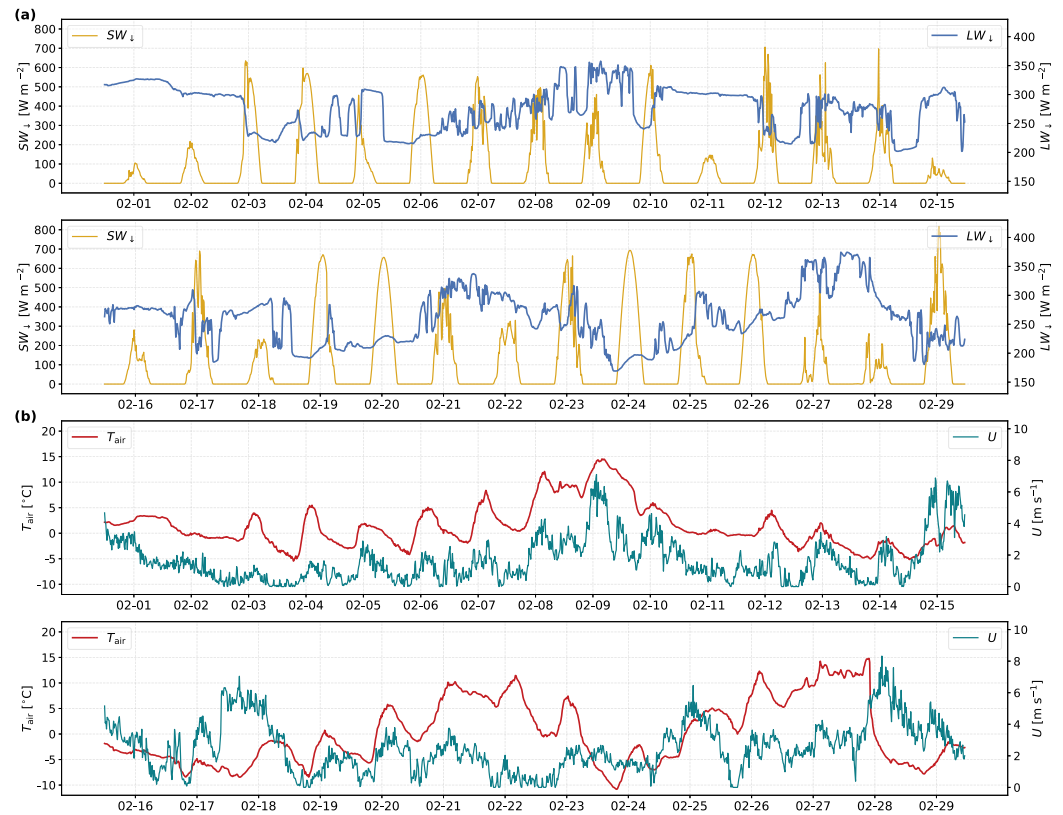


Figure A1. Time series of (a) total downwelling shortwave (SW_d) and longwave (LW_d) radiation, (b) ambient air temperature (T_{air}) and wind speed (U) in February 2024.

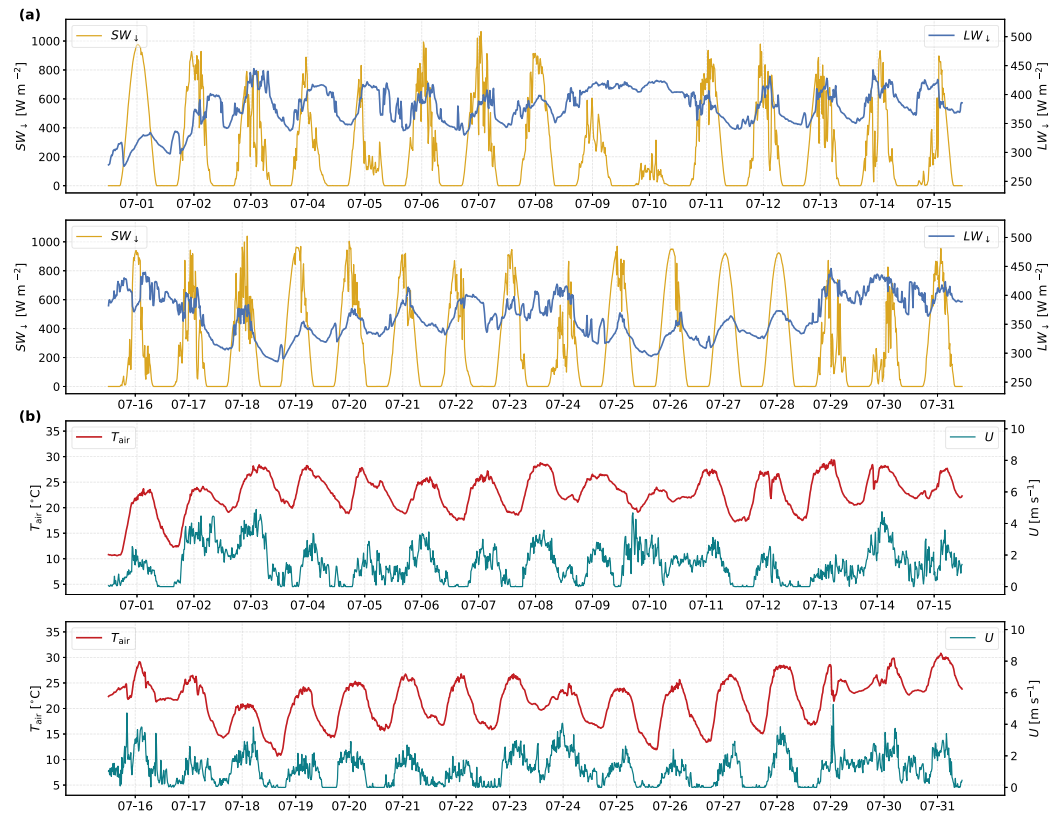


Figure A2. Time series of (a) total downwelling shortwave (SW_{\downarrow}) and longwave (LW_{\downarrow}) radiation, (b) ambient air temperature (T_{air}) and wind speed (U) in July 2024.

Data Availability Statement

The source code of the Weather Research and Forecasting (WRF version 4.3.3) model can be downloaded from <https://github.com/wrf-model/WRF/releases/tag/v4.3.3> (Skamarock et al., 2019). The ERA5 reanalysis data are publicly accessible from the Research Data Archive at the National Center for Atmospheric Research via <https://doi.org/10.5065/BH6N-5N20> (European Centre for Medium-Range Weather Forecasts, 2019). The observation data from the campaign, UCRC-Solar source code, and WRF output used to generate figures in the manuscript are archived at <https://doi.org/10.5683/SP3/FG4WC2> (Yin et al., 2024).

Acknowledgments

This work is funded by an Environment and Climate Change Canada Climate Action and Awareness Fund granted to ESK, JV and AAA. HY acknowledges the International Doctoral Tuition Scholarship (IDTS) from the University of Guelph. The authors further acknowledge the staff at the University of Western Ontario for their support in the project: Erika Hill (Geography and Environment technician), Mike Gaylard (Associate Director of Facilities, Faculty of Engineering), and Joan Ang (Manager, Energy and Carbon) for the PV electrical output data and Jessica Cordes (Engagement Coordinator) for facilitating access to the ACEB roof. The WRF simulations are supported by computational resources from the Digital Research Alliance of Canada. Open access publishing is covered by the University of Guelph Library.

References

- Appelbaum, J., & Bany, J. (1979). Shadow effect of adjacent solar collectors in large scale systems. *Solar Energy*, 23(6), 497–507. [https://doi.org/10.1016/0038-092X\(79\)90073-2](https://doi.org/10.1016/0038-092X(79)90073-2)
- Bird, R. E., & Hulstrom, R. L. (1981). Simplified clear sky model for direct and diffuse insolation on horizontal surfaces (Tech. Rep.). *Solar Energy Research Inst.(SERI)*.
- Booten, C., Kruijs, N., & Christensen, C. (2012). *Identifying and resolving issues in energypplus and doe-2 window heat transfer calculations (Tech. Rep.)*. National Renewable Energy Lab.(NREL).
- Broadbent, A. M., Krayenhoff, E. S., Georgescu, M., & Sailor, D. J. (2019). The observed effects of utility-scale photovoltaics on near-surface air temperature and energy balance. *Journal of Applied Meteorology and Climatology*, 58(5), 989–1006. <https://doi.org/10.1175/JAMC-D-18-0271.1>
- Brown, K. E., Baniassadi, A., Pham, J. V., Sailor, D. J., & Phelan, P. E. (2020). Effects of rooftop photovoltaics on building cooling demand and sensible heat flux into the environment for an installation on a white roof. *ASME Journal of Engineering for Sustainable Buildings and Cities*, 1(2). <https://doi.org/10.1115/1.4046399>
- Duffie, J. A., & Beckman, W. A. (1980). *Solar engineering of thermal processes*. Wiley.
- Environment and Climate Change Canada. (2022). National inventory report: Greenhouse gas sources and sinks in Canada. Retrieved from <https://publications.gc.ca/site/eng/9.506002/publication.html>
- Environment and Climate Change Canada. (2024). Past weather and climate. Retrieved from https://climate.weather.gc.ca/historical_data/search_historic_data_e.html
- European Centre for Medium-Range Weather Forecasts. (2019). Era5 reanalysis (0.25 degree latitude-longitude grid) [Dataset]. *Research Data Archive at the National Center for Atmospheric Research, Computational and Information Systems Laboratory*. <https://doi.org/10.5065/BH6N-5N20>

- Fraunhofer ISE. (2020). Photovoltaics report (Tech. Rep.). *Fraunhofer Institute for Solar Energy Systems*. Retrieved from <https://www.ise.fraunhofer.de/content/dam/ise/de/documents/publications/studies/Photovoltaics-Report.pdf>
- Google Earth. (2023). Map of the Amit Chakma engineering building on the campus of university of western Ontario. Retrieved from <http://www.google.com/earth/index.html>
- Green, M., Dunlop, E., Hohl-Ebinger, J., Yoshita, M., Kopidakis, N., & Hao, X. (2021). Solar cell efficiency tables (version 57). *Progress in Photovoltaics: Research and Applications*, 29(1), 3–15. <https://doi.org/10.1002/pip.3371>
- Hersbach, H., Bell, B., Berrisford, P., Hirahara, S., Horányi, A., Muñoz-Sabater, J., et al. (2020). The Era5 global reanalysis. *Quarterly Journal of the Royal Meteorological Society*, 146(730), 1999–2049. <https://doi.org/10.1002/qj.3803>
- Heusinger, J., Broadbent, A. M., Krayenhoff, E. S., & Weber, S. (2021). Adaptation of a photovoltaic energy balance model for rooftop applications. *Building and Environment*, 192, 107628. <https://doi.org/10.1016/j.buildenv.2021.107628>
- Heusinger, J., Broadbent, A. M., Sailor, D. J., & Georgescu, M. (2020). Introduction, evaluation and application of an energy balance model for photovoltaic modules. *Solar Energy*, 195, 382–395. <https://doi.org/10.1016/j.solener.2019.11.041>
- Hottel, H. C., & Sarofim, A. F. (1967). *Radiative transfer*. McGraw-Hill.
- Iqbal, M. (1983). *An introduction to solar radiation*. Academic Press.
- Jiang, T., Krayenhoff, E. S., Martilli, A., Nazarian, N., Stone, B., & Voogt, J. A. (2025). Prioritizing urban heat adaptation infrastructure based on multiple outcomes: Comfort, health, and energy. *Proceedings of the National Academy of Sciences*, 122(19). <https://doi.org/10.1073/pnas.2411144122>
- Jiang, T., Krayenhoff, E. S., Voogt, J. A., Warland, J., Demuzere, M., & Moede, C. (2023). Dynamically downscaled projection of urban outdoor thermal stress and indoor space cooling during future extreme heat. *Urban Climate*, 51, 101648. <https://doi.org/10.1016/j.uclim.2023.101648>
- Jones, A. D., & Underwood, C. P. (2001). A thermal model for photovoltaic systems. *Solar Energy*, 70(4), 349–359. [https://doi.org/10.1016/S0038-092X\(00\)00149-3](https://doi.org/10.1016/S0038-092X(00)00149-3)
- Kaldellis, J. K., Kapsali, M., & Kavadias, K. A. (2014). Temperature and wind speed impact on the efficiency of PV installations. Experience obtained from outdoor measurements in Greece. *Renewable Energy*, 66, 612–624. <https://doi.org/10.1016/j.renene.2013.12.041>
- King, D., Boyson, W., & Kratochvill, J. (2004). *Sandia photovoltaic array performance model* (Vol. 3535). SAND Report.
- Krayenhoff, E. S., & Voogt, J. A. (2007). A microscale three-dimensional urban energy balance model for studying surface temperatures. *Boundary-Layer Meteorology*, 123(3), 433–461. <https://doi.org/10.1007/s10546-006-9153-6>
- Ma, S., Goldstein, M., Pitman, A. J., Haghadi, N., & MacGill, I. (2017). Pricing the urban cooling benefits of solar panel deployment in Sydney, Australia. *Scientific Reports*, 7(1), 43938. <https://doi.org/10.1038/srep43938>
- Martilli, A., Clappier, A., & Rotach, M. W. (2002). An urban surface exchange parameterisation for mesoscale models. *Boundary-Layer Meteorology*, 104(2), 261–304. <https://doi.org/10.1023/A:1016099921195>
- Masson, V. (2000). A physically-based scheme for the urban energy budget in atmospheric models. *Boundary-Layer Meteorology*, 94(3), 357–397. <https://doi.org/10.1023/A:1002463829265>
- Masson, V., Bonhomme, M., Salagnac, J.-L., Briottet, X., & Lemonsu, A. (2014). Solar panels reduce both global warming and urban heat island. *Frontiers in Environmental Science*, 2. <https://doi.org/10.3389/fenvs.2014.00014>
- Matzarakis, A., Rutz, F., Mayer, H., et al. (2000). Estimation and calculation of the mean radiant temperature within urban structures. In *Biometeorology and urban climatology at the turn of the millenium (ed. by rj de dear, jd kalma, tr oke and a. auliciems): Selected papers from the conference icb-icuc* (Vol. 99, pp. 273–278).
- Millstein, D., & Menon, S. (2011). Regional climate consequences of large-scale cool roof and photovoltaic array deployment. *Environmental Research Letters*, 6(3), 034001. <https://doi.org/10.1088/1748-9326/6/3/034001>
- Nazarian, N., Krayenhoff, E. S., Bechtel, B., Hondula, D. M., Paolini, R., Vanos, J., et al. (2022). Integrated assessment of urban overheating impacts on human life. *Earth's Future*, 10(8), e2022EF002682. <https://doi.org/10.1029/2022EF002682>
- Porter, K. T., & Voogt, J. A. (2009). Multiscale assessment of urban emissivity. In *7th international conference on urban climate*. Retrieved from [http://www.ide.titech.ac.jp/~icuc7/extended_abstracts/pdf/384697-1-090123122807-002\(rev\).pdf](http://www.ide.titech.ac.jp/~icuc7/extended_abstracts/pdf/384697-1-090123122807-002(rev).pdf)
- Rowlands, I. H., Kemery, B. P., & Beausoleil-Morrison, I. (2011). Optimal solar-pv tilt angle and azimuth: An Ontario (Canada) case-study. *Energy Policy*, 39(3), 1397–1409. <https://doi.org/10.1016/j.enpol.2010.12.012>
- Sailor, D., Anand, J., & King, R. (2021). Photovoltaics in the built environment: A critical review. *Energy and Buildings*, 253, 111479. <https://doi.org/10.1016/j.enbuild.2021.111479>
- Salamanca, F., Georgescu, M., Mahalov, A., Moustauoui, M., & Martilli, A. (2016). Citywide impacts of cool roof and rooftop solar photovoltaic deployment on near-surface air temperature and cooling energy demand. *Boundary-Layer Meteorology*, 161(1), 203–221. <https://doi.org/10.1007/s10546-016-0160-y>
- Salamanca, F., Krpo, A., Martilli, A., & Clappier, A. (2010). A new building energy model coupled with an urban canopy parameterization for urban climate simulations—Part i. Formulation, verification, and sensitivity analysis of the model. *Theoretical and Applied Climatology*, 99(3), 331–344. <https://doi.org/10.1007/s00704-009-0142-9>
- Silva, J. P., Nofuentes, G., & Muñoz, J. V. (2010). Spectral reflectance patterns of photovoltaic modules and their thermal effects. *Journal of Solar Energy Engineering*, 132(4). <https://doi.org/10.1115/1.4002246>
- Skamarock, W. C., Klemp, J. B., Dudhia, J., Gill, D. O., Liu, Z., & Berner, J. (2019). A description of the advanced research WRF version 4. Tech. Note NCAR/TN-556+STR, 145.
- Sparrow, E. M. (2018). *Radiation heat transfer*. Routledge.
- Sparrow, E. M., Ramsey, J. W., & Mass, E. A. (1979). Effect of finite width on heat transfer and fluid flow about an inclined rectangular plate. *Journal of Heat Transfer*, 101(2), 199–204. <https://doi.org/10.1115/1.3450946>
- Stastny, A., Voogt, J. A., & Lao, J. (2023). A mobile traverse method to measure neighbourhood-scale microclimate [Conference Proceedings]. In L. L. Wang (Ed.), et al. (Eds.), *Proceedings of the 5th international conference on building energy and environment* (pp. 2821–2824). Springer Nature. https://doi.org/10.1007/978-981-19-9822-5_300
- Statistics Canada. (2024). Canada's population estimates. Retrieved from <https://www150.statcan.gc.ca/n1/daily-quotidien/230111/dq230111c-eng.htm?indid=4047-1&&indgeo=0>
- Tan, H., Kotamarthi, R., Wang, J., Qian, Y., & Chakraborty, T. C. (2023). Impact of different roofing mitigation strategies on near-surface temperature and energy consumption over the Chicago metropolitan area during a heatwave event. *Science of The Total Environment*, 860, 160508. <https://doi.org/10.1016/j.scitotenv.2022.160508>
- United Nations. (2018). The 2018 revision of the world urbanization prospects, population division of the united nations department of economic and social affairs (un desa). Retrieved from <https://www.un.org/en/desa/2018-revision-world-urbanization-prospects>
- Varga, N., & Mayer, M. J. (2021). Model-based analysis of shading losses in ground-mounted photovoltaic power plants. *Solar Energy*, 216, 428–438. <https://doi.org/10.1016/j.solener.2021.01.047>

- Walton, G. N. (1981). *Passive solar extension of the building loads analysis and system thermodynamics (blast) program* (Vol. 40, p. 41). United States Army Construction Engineering Research Laboratory.
- Walton, G. N. (1983). *Thermal analysis research program reference manual (Tech. Rep.)*. US, Department of Commerce.
- Wu, L. (1995). *An urban canopy layer surface energy balance climate model (Unpublished doctoral dissertation)* [PhD Thesis]. University of California.
- Yin, H., Krayenhoff, E. S., Voogt, J., Heusinger, J., & Aliabadi, A. A. (2024). Data and source code used for "simulation of tilted rooftop photovoltaic panels at city scale: Novel measurements, model development and application in WRF [Dataset]. *Borealis*. <https://doi.org/10.5683/SP3/FG4WC2>
- Zonato, A., Martilli, A., Gutierrez, E., Chen, F., He, C., Barlage, M., et al. (2021). Exploring the effects of rooftop mitigation strategies on urban temperatures and energy consumption. *Journal of Geophysical Research: Atmospheres*, 126(21), e2021JD035002. <https://doi.org/10.1029/2021JD035002>